PRODUCTION AND CHARACTERIZATION OF NANOFIBERS FROM
POLYCAPROLACTAM AND ETHYLENE-BUTYL ACRYLATE-MALEIC
ANHYDRIDE TERPOLYMER MIXTURE

A THESIS SUBMITTED TO
THE GRADUATE SCHOOL OF NATURAL AND APPLIED SCIENCES
OF
MIDDLE EAST TECHNICAL UNIVERSITY

BY

ERKAN BİBER

IN PARTIAL FULFILLMENT OF THE REQUIREMENTS
FOR
THE DEGREE OF DOCTOR OF PHILOSOPHY
IN
POLYMER SCIENCE AND TECHNOLOGY

APRIL 2010

Approval of the thesis:

PRODUCTION AND CHARACTERIZATION OF NANOFIBERS FROM POLYCAPROLACTAM AND ETHYLENE-BUTYL ACRYLATE-MALEIC ANHYDRIDE TERPOLYMER MIXTURE

submitted by **ERKAN BİBER** in partial fulfillment of the requirements for the degree of **Doctor of Philosophy in Polymer Science and Technology Department, Middle East Technical University** by,

Prof. Dr. Canan Özgen
Dean, Graduate School of **Natural Applied Sciences**   _____

Prof. Dr. Cevdet Kaynak
Head of Department, **Polymer Science and Technology**_____

Prof. Dr. Güngör Gündüz
Supervisor, **Chemical Eng. Dept., METU**   _____

Prof. Dr. Üner Çolak
Co-supervisor, **Nuc. Eng. Dept., Hacettepe U.**   _____

Examining Committee Members:

Prof. Dr. Ülkü Yılmazer
Chemical Eng. Dept., METU   _____

Prof. Dr. Güngör Gündüz
Chemical Eng.Dept., METU   _____

Prof. Dr. Erdal Bayramlı
Chemistry Dept., METU   _____

Prof. Dr. Zuhal Küçükyavuz
Chemistry Dept., METU.   _____

Prof. Dr. Ali Güner
Chemistry Dept., Hacettepe U.   _____

Date: ___29/04/2010___

I hereby declare that all information in this document has been obtained and presented in accordance with academic rules and ethical conduct. I also declare that, as required by these rules and conduct, I have fully cited and referenced all material and results that are not original to this work.

Name, Last name : Erkan Biber

Signature   :

ABSTRACT

PRODUCTION AND CHARACTERIZATION OF NANOFIBERS FROM POLYCAPROLACTAM AND ETHYLENE-BUTYL ACRYLATE-MALEIC ANHYDRIDE TERPOLYMER MIXTURE

Biber, Erkan

PhD, Department of Polymer Science and Technology

Supervisor: Prof. Dr. Güngör Gündüz

Co-Supervisor: Prof. Dr. Üner Çolak

April 2010, 91 pages

The impact strength of Nylon 6 was improved by adding Ethylene- n-Butyl acrylate- maleic anhydride (E-nBA-MAH) terpolymer with various concentrations from 0% (w/w) to 15% (w/w). The bare interaction energy between two polymers was investigated by using melting point depression approach utilizing both the Flory-Huggins (FH) theory and the Sanchez-Lacombe Equation of State (SL EOS).

The solution of the mixture was electrospun, and the effects of process parameters on the expected radii of nanofibers were investigated. The effects of process parameters such as polymer concentration in solution, electrical field, diameter of syringe needle, feed rate, and collector geometry on nanofibers were studied. The statistical analysis to relate these parameters on the diameter of nanofibers was carried out by using Johnson S_B distribution.

The ratio of elastic modulus to viscosity coefficient of nanofibers was worked out by using AFM and combined viscoelastic models. The experiments were carried out on single fiber. The ratio came out to be a function of nanofiber diameter and terpolymer concentration.

Isothermal crystallization kinetics and WAXS diffraction patterns of blends revealed and also SEM images supported that after 5% addition of elastomeric terpolymer, the interaction between the components of the blend gets weaker. The elastic modulus of the blend with 5% of terpoymer was greater than that of the neat Nylon 6, but the elastic modulus decreased for the blends containing more than 5% terpolymer.

ÖZ

POLİKAPROLAKTAM VE ETİLEN-BÜTİL AKRİLAT-MALEİK ANHİDRİT
TERPOLİMERİ KARIŞIMINDAN ELDE EDİLEN NANOFİBERLERİN
ÜRETİMİ VE ÖZELLİKLERİNİN BELİRLENMESİ

Biber, Erkan

Doktora, Polimer Bilmi ve Teknolojisi

Tez Yöneticisi: Prof. Dr. Güngör Gündüz

Ortak Tez Yöneticisi: Prof. Dr. Üner Çolak

Nisan 2010, 91 sayfa

Naylon 6 nın çarpma dayanımı, etilen-n-bütil akrilat-maleik anhidrit terpolimerini (E-nBA-MAH) ağırlıkça %0'dan %15'e değişen oranlarda katarak arttırılmıştır. İki polimer arasındaki tam etkileşim enerjisi, ergime noktası kayması yaklaşımı ile Flory-Huggins (FH) kuramı ve Sanchez-Lacombe Durum denklemi (SL EOS) kullanılarak araştırılmıştır.

Süreç değişkenlerinin elektro eğirme yolu ile elde edilen nanofiberlerin çapları üzerine olan etkileri incelenmiştir. Bu kapsamda çözeltideki polimer derişimi, elektriksel alan, şırınga çapı, besleme hızı ve toplaç geometrisi gibi süreç değişkenlerinin nanofiberler üzerine olan etkileri araştırılmıştır. Johnson SB dağılımı kullanarak istatistiksel analiz yapılmış ve çap boyunun süreç değişkenlerine bağımlılığı matematiksel olarak ifade edilmiştir.

Nanofiberlerin elastik modülüne viskozite katsayısı oranı Atomik Kuvvet Mikroskobu ve birleşik viskoelastik modeller kullanarak, bulunmuştur. Bu oran, nanofiber çapı ve terpolimer derişimine bağlı olduğu bulunmuştur.

Karışımların eşısıl kristallenme kinetiği ve WAXS kırınım deseninin gösterdiği ve ayrıca SEM görüntülerinin de desteklemiş olduğu deneysel sonuçlardan anlaşıldığı üzere % 5 den daha fazla terpolimerin katılması durumunda karışımın bileşenlerinin arasındaki etkileşim zayıflamaktadır. %5 terpolimerli karışımın elastik modülü, saf Naylon 6 nınkinden daha fazladır, fakat 5%'den daha fazla terpolimer içeren karışımların elastik modülü düşmektedir.

Anahtar sözcükler: Nylon 6, polimer karışımı, çarpma, Flory-Huggins, Sanchez-Lacombe, elektro eğirme, ölçeklenme, viskoelastisite.

To The Whole that made me as myself

ACKNOWLEDGEMENTS

TABLE OF CONTENTS

LIST OF TABLES

LIST OF FIGURES

FIGURES

NOMENCLATURE

^{o}C	Celsius
cm	Centimeter
d	Diameter
E	Electrical field
G	Rate of crystallization
GPa	Gigapascal
H_f	Heat of fusion
K	Kelvin
K	Avrami crystallization rate constant
MPa	Megapascal
m	Temperature dependent coefficient
$\vec{n}$	Normal vector
nm	Nanometer
M	Molecular weight
M_w	Weight average molecular weight
P	Pressure
P^{*}	Characteristic pressure
Q	Feed rate
R	Universal gas constant
r	Characteristic length
υ^{*}	Characteristic volume
T^{*}	Characteristic temperature
T	Temperature
t	Time
T_m^{o}	Equilibrium melting temperature
V	Volume

U	Electrical field energy
X	Percent crystallization
α	Thermal expansion coefficient
μm	Micrometer
B_{ij}	Interaction energy density
ε	Permittivity of system
ΔE	Crystallization activation energy
Δh_{iu}	Heat of Enthalpy
Δg	Free energy of mixing per volume
τ_o	Relaxation time
$\Delta \mu_1$	Chemical potential difference
ΔP_{ij}^{*}	Bare interaction energy
ϕ_i	Volume fraction
φ	Nonlinear parameter
δ	Johnson S_B distribution parameter
χ	Turnbull-Fisher equation parameter
χ	Parameter for electrical field magnitude
AFM	Atomic force microscope
DSC	Differential scanning calorimetry
E-*n*BA-MA	Ethylene-*n*Butyl Acrylate-Maleic Andhyride Terpolymer
FH	Flory-Huggins theory
HW	Hoffman-Weeks plots
LDPE	Low density polyethylene
SEM	Scanning electron microscope
SL-EOS	Sanchez-Lacombe equation of state theory
WAXS	Wide angle X-Ray scattering

CHAPTER 1

INTRODUCTION

Nanotechnology can be defined as development of systems in course of the nanometer (1 to 100 nm) length scale. It has been a new technological field in the intersection of basic scientific fields, i.e. chemistry, biology, and physics. The main objective in this novel area has been to exploit new properties and phenomena at this scale since *Richard Feynman*, Nobel Prize winner and the pioneer of nanometer scale systems defined nanotechnology in 60s.

Nanometer (from Greek νάνος, nanos, *dwarf*; μετρώ, metró, *count*) is one billionth of a meter (10^{-9} m). For comparison, Van der Walls radius of C atom is 0.17 nm and C-C bond length is 0.146 nm. A cube that has the side of 10 nm would contain about 244,000 carbon atoms. The diameter of a human hair is 1000 times greater than 10 nm. Catalyzing proteins in cells are about 1 to 20 nm in size.

There are five reasons why nanometer scale is important. Firstly, electronic wavelike properties are affected by manipulations within matter, so fundamental physical properties can be adjusted. Secondly, wavelength interactions between materials gain importance at this level so that various opto-electronic applications could be achieved. Thirdly, near molecular size surface tension and electromagnetic effects enable harder and less brittle material tailoring. Fourthly, systematic organization at nano scale is a key factor of biological area, such as realistic artificial components and assemblies inside cells. Lastly, high surface to volume ratio makes nano

devices ideal for use in reacting mechanisms, drug delivery, energy storage, nanosensors, filtration, and composite materials.

Nanofibers are important structures in nanotechnology. High surface area (10^3 times greater than microfiber) allows the use of functional flexibility and superior mechanical properties in many applications. Nanofibers can be produced by drawing, template synthesis, phase separation, self assembly, and electrospinning. Electrospinning process is widely used for its ease of controllability.

Electrospinning is a process that converts polymeric melt or solution into nano or submicron fibers. Basic components of the process are (i) a high voltage DC power supply, (ii) a conductive collector, and (iii) a capillary tube that contains polymeric melt or solution. High voltage DC power supply generates high electrical field between collector and needle of container. Electrically charged jet that is held by its surface tension, purges out of the needle. The mutual repulsion forces that are generated by electrical forces and the contraction forces that are generated by surface tension try to hold the droplet at equilibrium in hemispherical shape. However, as the intensity of electrical field increases, the hemispherical shape elongates and becomes a cone that is called "Taylor Cone". As charged jet travels further, it takes the form of a straight line that is named as stable region. Then, it goes under unstable regime which is of conical shape. Fibers with various diameters (from submicron to nanometers) deposit at the collector surface with non-woven mat morphology.

Electrospinning has many parameters that interact with each other and affect the resultant nanofibers. They can be classified into three main groups: (i) processing parameters, (ii) solution parameters, and (iii) ambient parameters. Processing parameters are applied voltage, tip-to-collector distance, shape and design of collector, feed rate of material that is a function of capillary pressure inside tube. Solution parameters are concentration, viscosity, surface tension, dielectric properties, solubility, interaction energies, and the volatility of solvent. Ambient parameters are

humidity, pressure, temperature, type of atmosphere, and velocity of atmosphere presents around [1].

Parameters of electrospinning process affect morphology of produced nanofibers as well as each other. Such characteristics make it intricate to investigate the effect of parameters individually. Tip-to-collector distance has an effect on electrical field as well as travel distance where the jet finds enough time to solidify. Concentration and viscosity affect the physical entanglement of polymer chain, but also they are affected by volatility of the solvent and ambient parameters. Surface tension is influenced by temperature, but solubility and volatility are both affected by temperature and pressure.

Various materials including polymers, ceramics, and composites can be used to produce nanofibers by electrospinning. One of the polymeric materials that can be used is Nylon 6 (or polyamide 6 or poly(ε-Caprolactam)). Nylon 6 is an engineering thermoplastic and has high tear and abrasion resistance, low friction coefficient, high strength, and elasticity. On the other hand, it has relatively poor notched impact strength, high moisture sensitivity, and relatively high price. The derivatives of low density polyethylene (LDPE) is the one of the best materials to blend with Nylon 6 to enhance its mechanical properties due to low cost, low coefficient of friction, lightweight, high strength, high barrier properties to moisture, good optical properties, and ease of processing. Compatible blend of the toughening engineering plastics is usually achieved by modifying the chemically inert polyolefin with maleic anhydride, acrylic acid, or glycidyl methacrylate to interact with polyamide [2, 3].

Mechanical characterization of nanofibers can be performed as non-woven mats or single fiber. Due to very small diameters, single nanofiber characterization is a challenge with existing test techniques. Impact modified nanofibers can be mechanically characterized in order to investigate the impact properties or viscoelastic behavior. Viscous property helps the polymeric system to absorb the excess impact energy in a short time. Impact

3

modification means, in other words, to enhance the viscous property of polymer [4].

Spring-dashpot models give brief information about polymeric material viscoelastic characteristics. Spring element is responsible for energy storage as in solid material deformation and dashpot element is responsible for energy dissipation as in viscous material deformation. Under impact coonditions, that is sudden loading, spring element is not able to store in such a short time. Dashpot element should absorb the excess energy before the failure. In other words, one should enhance the "dashpot characteristics" of polymeric material to bear the sudden loads.

The aim and originality of the study were to obtain impact modified Nylon 6 nanofibers by electrospinning. The study involved the compatibility study of Nylon 6 and ethylene-butyl acrylate-maleic anhydrite terpolymer. Theoretical analysis based on the data obtained from melting point depression was developed to explore the compatibility of the components. The aim in the experimental part was to investigate the effect of processing parameters on the diameter of the fibers and also on the viscoelastic properties of fibers.

CHAPTER 2

LITERATURE SURVEY AND THEORY

Review of the literature for electrospinning, blending, statistical distribution analysis, and mechanical characterization for electrospun nanofibers is done in this section. Furthermore, theoretical information is given for blending, crystallization kinetics and viscoelastic mechanical properties.

2.1 Electrospinning

Electrospinning is a process that converts polymeric solution or melt into nanofibers under high DC voltage as seen in Fig. 2.01.

The figure shows main components of electrospinning process, the container with a pipette or needle of small diameter, the metal collector, and the high voltage DC power supply. The electrified polymeric jet elongates at the beginning of the stability region to form Taylor cone in the z-direction, and then travels at the region of instability onto collector inside the instability cone envelope It further undergoes elongation under gravitational field ($\vec{g}$) and electrical field ($\vec{E}_{\infty}$) while solidifying due to evaporation of solvent. Nanofibers collected can be usually examined by using SEM micrographs [5].

The parameters which affect electrospinning and the resulting fibers are mainly polymer solution parameters, processing conditions, and ambient conditions as mentioned earlier. Solution parameters affect the chain entanglement of polymer, which is actually affected by the concentration and the viscosity of the solution, and surface tension.
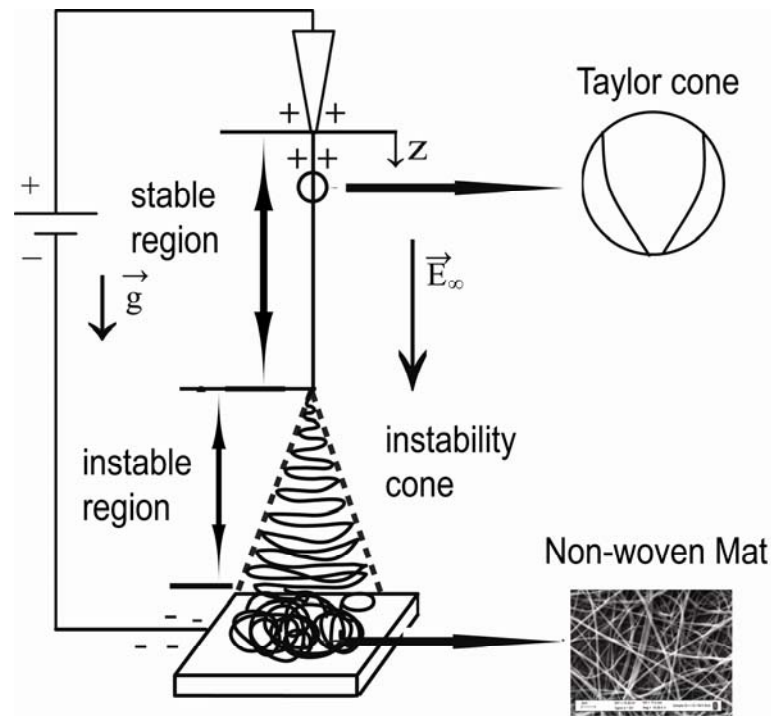
Figure 2.01 Scheme of electrospinning process.

Surface tension changes with temperature, the dielectric properties of solvent, solubility, and the volatility of the solvent which is also a function of temperature and pressure. Processing conditions are voltage, distance between tip-to- collector and its geometry, and the feed rate of solution stock. Ambient parameters are humidity, pressure, temperature, and type of atmosphere. Since these parameters mutually depend on each other the investigation of their effect on nanofibers is of real challenge [1].

There have been some parametric studies of electrospinning in the past [6]. The effect of average molecular weight (Mw) of poly(vinylalcohol)

(PVA) [7], solution properties of the egg albumen (EA) and of poly(ethylene oxide) such as viscosity, surface tension, and electrical conductivity have been studied [8]. Cui et al. studied the morphology and the diameter of electrospun poly(3-hydroxybutyrate-co-3-hydroxyvalerate) (PHBV) nanofibers by varying processing parameters [9]. The effect of electrical current on nanofiber [10, 11], and the varying needle diameter on the diameter of poly(methyl methacrylate) (PMMA) nanofibers were also investigated [12].

The collector design results in oriented nanofibers [13, 14]. The wheel-like collector design [15] is reported to produce oriented nanofibers. The extent of the orientation gets higher at the direction of stretching by accelerating the rotating wheel using polarized Fourier transform infrared spectroscopy (FT-IR) [16]. It is also possible to produce oriented single fiber by using microfludic device [17].

Electrospun nanofibers can be used in drug delivery [18], tissue engineering [19, 20], and composite materials [21, 22]. Nanofiber composites find large applications such as conductive composites [23], mechanically reinforced composites [24], and the ceramic-polymer hybrid composites [25].

2.2 Blending

Blends are made to make materials with new properties which utilize the physical properties of the components. Usually reinforced materials are obtained from blends. The homogenous polymer blends should be compatible with each other to be used in applications. Incompatible mixture blends have inhomogeneous characteristics and their material properties change locally. There are several ways to investigate compatibility of polymers. Melting point depression evaluation has been widely used to examine polymer/polymer interactions to eradicate the effects of morphology and crystal thickness of polymers [26-37]. Interaction energy between polymers can be calculated using either the Flory-Huggins theory (FH) or the

lattice-fluid theory of Sanchez-Lacombe (SL-EOS) which are both based on the melting point depression method [38-41].

Equation of state approach to determine the compatible blend condition has some advantages [27]. Effects of crystalline structures on non-equilibrium melting or experimental melting conditions can be excluded by taking the concept of the equilibrium melting temperature into account. Equilibrium melting temperature can be defined as the temperature to complete the melting of the large polymeric crystals with high molecular weight where end group effects are neglected. Blending technique also affects the crystal structures of mixture [42].

The effect of crystalline structure on blending can be investigated by isothermal crystallization kinetics [43-45] or nonisothermal crystallization kinetics [46, 47] or both [48, 49]. In isothermal crystallization, Avrami, Tobin, Malkin models [50] are used, Avrami model gives markedly consistent results [43]. It is reported that Avrami parameters give information on the rate of crystallization, the activation energy of crystallization, and crystallization structure depending on blending [47].

It is obvious that Nylon 6 preserves the commercial importance in polymer industry [51] and application areas can be further increased by modification of properties of Nylon 6.

Nylon 6 has polymorphous structure [52, 53], the phases α and γ. The α-phase is monoclinic and the hydrogen-bonded sheets are shared alternatively antiparallel to the chain. The γ-phase is a metastable phase with a variable degree of disorder or stacking faults. It includes stacking of parallel and antiparallel chains, the paracrystalline disorder, faults in the hydrogen bonded sheet-like setting, and hydrogen-bonded layers perpendicular instead of parallel to the chain axis. Furthermore, the α- phase is suggested to have folded chains [54] and it is more stable than the γ-phase.

2.3 Blending Theories

2.2.1 Flory-Huggins Theory (FH Theory)

In terms of the classical FH theory, the free energy of mixing per volume (Δg) can be expressed as follows,

$$\Delta g = \sum \sum_{i<j} B_{ij} \phi_i \phi_j + RT \sum_i \frac{\phi_i}{\upsilon_i} \ln \phi_i \qquad (2.01)$$

where B_{ij} is interaction energy density. Chemical potentials of polydisperse systems are defined in the following form at constant temperature and pressure,

$$\Delta \mu_i = \upsilon_i \left(\Delta g + \left(\frac{\partial \Delta g}{\partial \phi_i} \right)_{\phi'} \right) - \sum_j \phi_j \left(\frac{\partial \Delta g}{\partial \phi_j} \right)_{\phi'} \qquad (2.02)$$

After some algebra for binary mixture, it yields

$$\Delta \mu_1 = RT \left(\ln \phi_1 + 1 - \frac{\upsilon_1}{\upsilon} \right) + \upsilon_1 \phi_1^2 B_{12} + \phi_1 \frac{dB_{12}}{d\phi_1} \qquad (2.03)$$

$\Delta \mu_2$ can be found by interchanging the indices 1 and 2. The chemical potential of the crystalline phase can be written as [55],

$$\Delta \mu_i = -\Delta h_{iu} \left(1 - \frac{T_{mb}^o}{T_m^o} \right) \upsilon_i \qquad (2.04)$$

where Δh_{iu} is the enthalpy of fusion per volume and T_{mb}^o and T_m^o are the equilibrium melting temperature for the mixture and for the pure state, respectively. At equilibrium, the chemical potential of the crystalline and liquid phases should be identical. The following result is obtained by equating $\Delta \mu_1$ from Eq. 2.03 and Eq. 2.04 by assuming that B_{ij} is not a function of ϕ_i, and also the combinatorial entropy contribution, $RT\left(\ln \phi_1 + 1 - \dfrac{\upsilon_1}{\upsilon} \right)$, is negligible [41],

$$T_{mb}^o = T_m^o + \frac{B_{12}T_m^o}{\Delta h_{2u}}\left(1-\phi_2\right)^2 \tag{2.05}$$

where component 2, ϕ_2, represents the crystalline component in binary mixture.

2.2.2 Sanchez-Lacombe Equation of State Theory (SL EOS Theory)

The Sanchez-Lacombe equation of state (SL EOS) has the following close form,

$$\tilde{\rho}^2 + \tilde{P} + \tilde{T}\left[\ln(1-\tilde{\rho}) + \left(1 - \frac{1}{r}\right)\tilde{\rho}\right] = 0 \tag{2.06}$$

where, $\tilde{P} = P/P^*$, $\tilde{T} = T/T^*$, and, $\tilde{\rho} = 1/\tilde{\upsilon} = \rho/\rho^*$ are thermodynamic variables. Here, asterisks denote characteristic variables, while bars denote reduced variables. P^* is characteristic pressure, υ^* is characteristic volume, T^* is characteristic temperature, and ρ^* is characteristic density defined as $\rho^* = P^*M/RT^*r$ where r is polymer chain length, M is molecular weight

which must be replaced by the weight average molecular weight (M_w) for polydisperse components.

The characteristic thermodynamic variables are applicable to linear mixing rule for both random copolymers and homogenous blends.

$$P^* = \sum \phi_i P^*_i - \sum \sum_{i<j} \phi_i \phi_j \Delta P^*_{ij} \qquad \Delta P_{ij} = \left(\sqrt{P^*_i} - \sqrt{P^*_j} \right)^2$$

$$\frac{1}{\rho^*} = \sum \frac{w_i}{\rho^*_i}$$

$$\frac{1}{\upsilon^*} = \sum \frac{\phi_i}{\upsilon^*_i}$$

$$T^* = \frac{P^* \upsilon^*}{R}$$

$$\frac{1}{r} = \sum \frac{\phi_i}{r_i}$$

(2.07)

where ΔP^*_{ij} is bare interaction energy for the blend, w_i is weight fraction of ith component, and ϕ_i is volume fraction of ith component. In this theory, B_{ij} can be replaced by ΔP^*_{ij}.

At equilibrium, the chemical potential should be equal to that of the crystalline component, and details can be found elsewhere [41],

$$-\frac{\Delta h_{2u}}{RT^o_{mb}} \left(1 - \frac{T^o_{mb}}{T^o_m} \right) = \frac{\tilde{\rho}}{RT^o_{mb}} \Delta P^* (1 - \phi_2)^2$$

$$+ \left(\frac{1}{r_2^o \upsilon_2^*} - \frac{1}{r\upsilon^*} \right) + \frac{1}{r_2^o \upsilon_2^*} \ln \left(\frac{\tilde{\rho} \phi_2}{\tilde{\rho}_2} \right)$$

$$+ \frac{1}{\upsilon_2^*} \left(\frac{(1 - \tilde{\rho}) \ln(1 - \tilde{\rho})}{\tilde{\rho}} - \frac{(1 - \tilde{\rho}_2) \ln(1 - \tilde{\rho}_2)}{\tilde{\rho}_2} \right)$$

(2.08)

2.2.3 Isothermal Crystallization Kinetics

The Avrami equation is applied to evaluate the isothermal crystallization of the polymer blends [56],

$$X(t) = 1 - \exp(-Kt)^n \tag{2.09}$$

or,

$$\log\{\ln[1 - X(t)]\} = n\log t + \log K \tag{2.10}$$

where X(t) is weight fraction of crystallized material in crystallization time t, K is Avrami crystallization rate constant, and n is Avrami exponent. X(t) is calculated by the ratio of the area of melting peak at time t to total measured area. K and n values can be found from the intercept, and slope of $\log\{\ln[1 - X(t)]\}$ vs. log t plot, respectively.

The percent crystallinity (X_C) can be calculated from

$$X_c = \frac{\int_0^t \left(\frac{dH_f}{dt}\right)dt}{\int_0^\infty \left(\frac{dH_f}{dt}\right)dt} \tag{2.11}$$

where H_f is heat of fusion. For Nylon 6, the value of heat of fusion of perfectly crystalline material (i.e. $\int_0^\infty (dH_f/dt)dt$), is about 188.1J/g. The maximum crystallization time t_{max} corresponds to the time when derivative of the heat flow rate with respect to time is equal to zero i.e. $dQ(t)/dt = 0$,

$$t_{max} = [(n-1)/nK]^{1/n} \tag{2.12}$$

12

Another important parameter is the half-time of crystallization (i.e. $t_{1/2}$) which is defined as the duration of the time from onset of the crystallization until the completion of 50% of the crystallization process, that is,

$$t_{1/2} = \ln\left(2/K\right)^{1/n} \tag{2.13}$$

The rate of crystallization G is defined as the reciprocal of $t_{1/2}$,

$$G = t_{1/2}^{-1} \tag{2.14}$$

Since crystallization process is thermally activated, crystallization rate parameter K can be approximately described by [57],

$$K^{1/n} = k_o \exp(-\Delta E / RT_c) \tag{2.15}$$

or

$$(1/n)\ln K = \ln k_o - (\Delta E / RT_c) \tag{2.16}$$

where k_o is temperature independent preexponential coefficient, R is the gas constant, and ΔE is activation energy for crystallization. The activation energy ΔE can be obtained from the slope of $(1/n)\ln K$ vs. $1/RT_c$ plot.

The dependence of growth rate G on crystallization temperature T_c, is given by the Turbull-Fisher equation given below [58],

$$\ln G = \ln G_o - \frac{\Delta E^*}{kT_c} - \frac{\Delta F^*}{kT_c} \tag{2.17}$$

13

where G is the spherulite growth rate, T_c is the crystallization temperature, ΔE^* is the activation energy for transporting a chain segment from the super-cooled state into crystalline phase, and ΔF^* is the free energy of formation of a nucleus at the critical size. Here k, is Boltzmann constant and G_o is preexponential constant. At high temperature, the nucleation term $\Delta F^*/kT_c$ will be dominant. At high temperatures, when crystallization temperature T_c approaches the melting temperature T_m, the expression becomes,

$$\ln G = \ln G_o - \frac{\Delta F^*}{kT_c} \tag{2.18}$$

or [59],

$$\ln G = \ln G_o - \frac{\chi T_m^o}{T_c^2 \left(T_c - T_m^o \right)} \tag{2.19}$$

where, χ is a parameter concerning heat of fusion and interfacial free energy, T_m^o is equilibrium melting temperature given by Hoffmann [92]. Lin obtains the following expression from Eq.2.10, 2.14 and 2.19 [59],

$$\log t_{max} = A - \frac{B}{2.303 T_c^2 \left(T_c - T_m^o \right)} \tag{2.20}$$

where, A and B are constants.

14

2.4 Statistical Distribution Analysis

The distribution of nanofibers gives information about the effects of process parameters on product [60]. The concentration of the solution of poly(ethylene oxide) (PEO) and voltage on the morphology and the distribution of fiber diameters were studied by Dogheri et. al. [61]. The needle also has influence on nanofibers [61].

Various distribution functions can be used to analyze diameter distribution of fibers [60]. It is demonstrated that 4 parameter log-normal or Johnson SB distribution function proposed by Johnson is superior to many two-parameter function in terms of curve fitting capacity including bimodal characterized distributions [63]. It uses standardized values of the parameters.

2.5 Mechanical Characterization

Electrospun nanofibers can mechanically be characterized by many methods [64-66], and Atomic Force Microscopy (AFM) is a very powerful technique in finding out the mechanical properties including viscoelastic behavior of nanofibers. AFM analysis gives information about the impact strength of polymers [4] as compared with traditional Dynamic Mechanical Analysis (DMA) [67] together with tensile testing [68].

AFM is capable to measure the properties under static loading at constant rate if vibrational force is excluded [69]. One can measure the dynamic mechanical properties of polymer accurately by applying oscillation on the substrate [70, 71]. The Hertz model was introduced to measure the frequency-dependent storage and loss moduli of polymeric material [72]. Contact models Sneddon's and JKR were tested for various indentation depths besides Hertzian model by Chizhik et. al [73].

15

Mechanical properties of nanofibers electrospun from many polymer blends such as Bombyx mori silk/Poly(ethylene oxide) (PEO) nanofibers [74], Poly(butylene terephthalate) polymer reinforced by multi-walled carbon nanotubes [75], and polypropylene/ethylene–propylene copolymer blends (PP/EP) were also investigated [76].

Viscoelastic properties using the Maxwell and the Kelvin-Voigt models were evaluated by AFM with good correlation by using the measurements of conical intender loading [77] and creep response of polymer [73]. In this study, aligned electrospun Nylon 6 nanofibers and its blends with impact modifier polymer Poly (ethylene- *n*-butyl acrylate-maleic anhydride) (E-*n*BA-MAH) terpolymer at various concentrations from 0 to 15 wt% were tested by using AFM. Then the data were used in combined viscoelastic models (i.e. Maxwell and Kelvin-Voigt) to determine the relaxation time of a single nanofiber.

CHAPTER 3

MATERIALS AND PROCEDURES

This chapter deals with the polymers used in the study, mixture preparation and experimental procedures, and data analysis techniques.

3.1 Polymers

Polymers used in this study are Nylon 6 (trade name Teklamid 6) from Polyone (M_W=13600 g/mol, ρ=1.13 g/cm3), Poly (ethylene- n-butyl acrylate-maleic anhydride) (*E-nBA-MAH*) terpolymer (trade name Lotader 2210) from Arkema Chemicals (M_v=33900 g/mol, ρ=0.94 g/cm^3). The terpolymer contains 91 weight (wt) % ethylene, 6 wt % acrylate, and 3 wt % maleic anhydride. Chemical formula of *E-nBA-MAH* terpolymer is given in Fig. 3.01. The *E-nBA-MAH* terpolymer has mainly the structure of low density polyethylene (LDPE). *n*-Butyl acrylate reduces the crystallinity of the system, and maleic anhydride can react with the amine group of Nylon 6 to provide stability [78].

3.2 Sample Preparation

Blends were prepared in solution phase. Nylon 6 was dissolved in formic acid (MERCK A.G.), E-*n*BA-MAH was dissolved in hot xylene (MERCK A.G.), and 2-propanol (MERCK A.G.) was used as co-solvent to provide miscibility of formic acid and xylene. The solution was then electrospun at 20 kV with a tip-to-collector distance of 10 cm. The electrospun nanofiber mats were dried at 40 $^{\circ}$C under vacuum (400 Torr) to let the traces of the solvents evaporate.
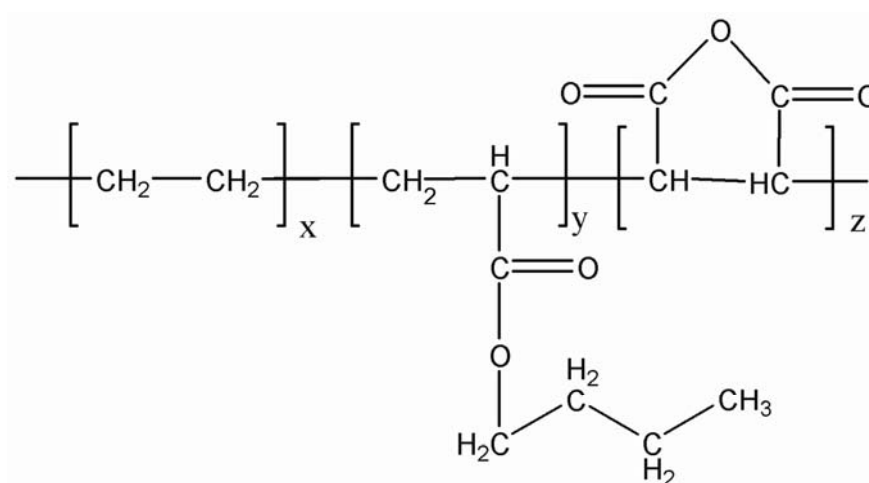
Figure 3.01 Chemical formula of E-*n*BA-MAH.

3.2.1 Solution Preparation

E-*n*BA-MAH was blended with Nylon 6 of concentration % (w/w) 0, 5, 10, and 15. Nylon 6 solution (40 % w/v) was prepared by using formic acid. The solutions of terpolymer were prepared at concentrations of 5% (w/v) and 10% (w/v) in hot xylene at 60 $^{\circ}$C.
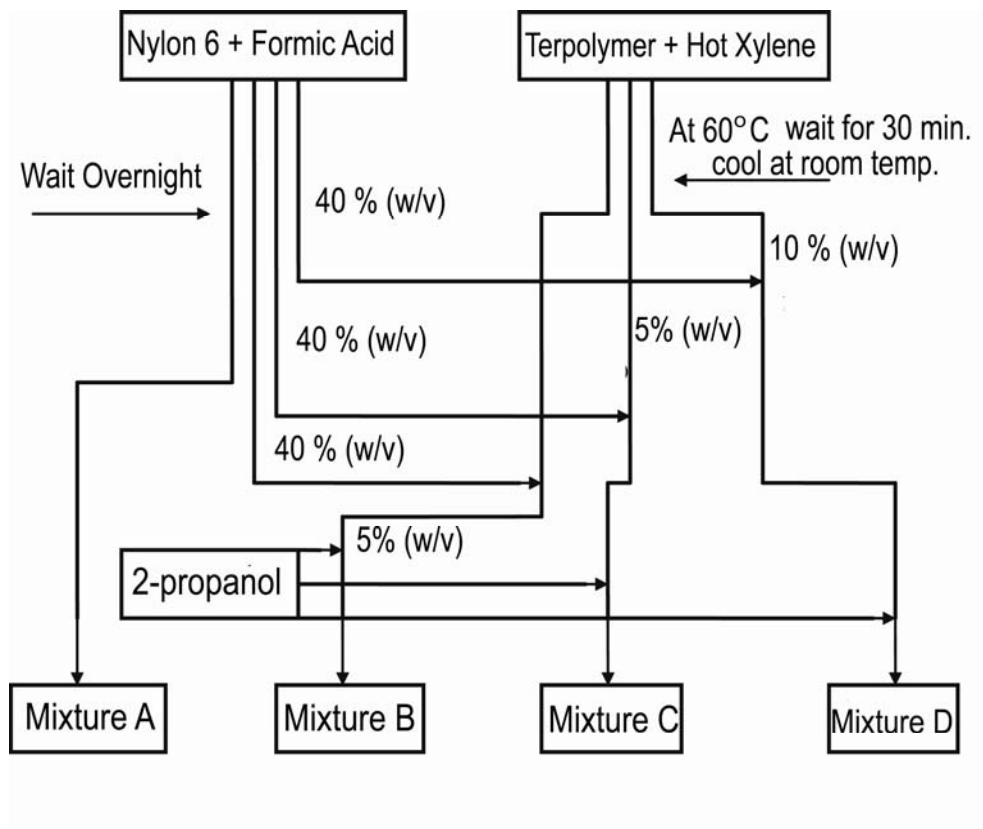
Figure 3.02 The flow chart and contents of the mixtures.

Table 3.01 Mixture contents.

Content		Mixture A	Mixture B	Mixture C	Mixture D
E-*n*BA-MAH	(g)	0	5	10	15
Nylon 6	(g)	100	95	90	85
Formic Acid	(ml)	100	62	47	52
Xylene	(ml)	0	26	41	37
2-Propanol	(ml)	0	14	10	11
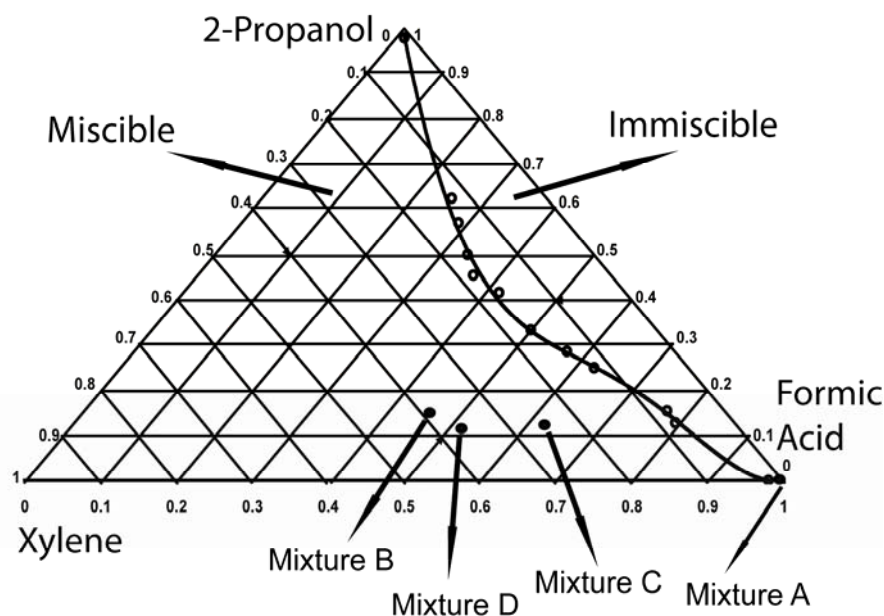
Figure 3.03 Miscibility map of solvent system.

Blends were prepared by 5 % (w/w), 10 %(w/w) and 15 (w/w) terpolymer in Nylon 6. In order to prepare homogenous blends, 2-propanol was added in 1:9 volume ratio into formic acid. One set of solution contained only Nylon 6 without terpolymer. The set of mixtures was labeled as Mixture A, Mixture B, Mixture C, and Mixture D. They have 0%, 5%, 10%, and 15% terpolymer content, respectively. The flow chart of mixture preparation is given in Fig. 3.02. Table 3.01 gives the content of mixtures.

The solubility range of the solvents based on volume percent and solvents in mixtures are seen in Fig.3.03. The curve in the figure was obtained from solubility data. Each point on the curve corresponds to the point where clarity is lost and the mixture becomes turbid as seen by human eye by the points. The prepared polymeric mixtures A, B, C, and D with compositions of 0, 5, 10, and 15 %, respectively are in miscible zone.

The miscibility map was obtained to acquire the homogenous solvent mixture which helps the polymers to get the vicinity of each other. Nylon 6 has polar nature and E-nBA-MAH terpolymer has non-polar nature. This leads the melt blend not to be mixed properly. But, the solvent system

proposed here overcomes the shortcoming of immiscibility of the polymeric blends and blending in solution phase was achieved.

3.3 The Setup for Electrospinning

The high voltage source of electrospinning setup is Gamma ES30 (Gamma High Voltage Research Company). The process was carried out at room conditions inside a protective guard made of Poly (methyl methacrylate) (PMMA). The positive pole of high voltage was attached either to the needle of syringe or dipped into the solution cell. The negative pole was attached to the metal collector covered by aluminum foil. The high voltage source was grounded. The setup is given in Fig. 3.04.
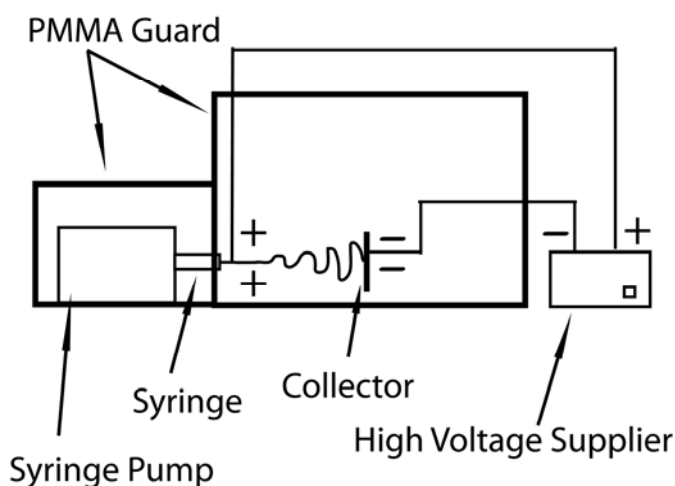
Figure 3.04 Experimental setup of electrospinning.

The solution cell is either a micropipette which has 0.5 mm of diameter, or syringe with a needle, the cell part of the syringe is 0.3 mm in diameter and 8 mm in length. Solution in micropipette comes down due to gravity at vertical position, but when syringe is used in horizontal position a pump is needed (New Era NE-1600) for better control of fluid flow.

3.4 Wide Angle X-Ray Scattering (WAXS)

Nanofibers obtained from neat Nylon 6, and 5% and 10% *E-nBA-MAH* terpolymer containing blends were kept at $40^{\circ}C$ in a drier. Another 10% *E-nBA-MAH* terpolymer was dried under vacuum (400 Torr) at room temperature in order to detect the effect of heat on WAXS peaks. WAXS tracks were taken by using (Rigaku D/MAX 2200) X-ray diffractometer, which has monochromic Cu resource (A4 1L-Cu / 60 kV, 2.0 kW).

3.5 Differential Scanning Calorimetry (DSC)

The changes in the melting point were determined by using Differential Scanning Calorimetry (DSC) (TA Q200 Differential Scanning Calorimeter). Nanofiber samples that were heated to 250 $^{\circ}C$ at 100 $^{\circ}C$/min were kept at this temperature for 5 minutes to eliminate any previous thermal history, and then they were cooled down to the four predetermined crystallization temperatures (T_c) of 186, 188, 190, 192 $^{\circ}C$ at a cooling rate of 150 $^{\circ}C$/min. The samples were kept at T_c for 20 minutes, which is necessary for the DSC signals to return to the baseline. The samples were then quenched to 50 $^{\circ}C$ with a cooling rate of 150 $^{\circ}C$/min. After 5 minutes of infusion at 50 $^{\circ}C$, the samples were heated back up to 250 $^{\circ}C$ at a rate of 10 $^{\circ}C$/min to obtain the signals.

3.6 Scanning Electron Microscopy (SEM)

QUANTA 400F Field Emission Scanning Electron Microscope (SEM) operated at 30 000 kV was used for SEM images. It has 1.2 nm resolution. The specimens were prepared as follows; solution of each mixture (0%, 10% and 15%) were poured onto glass slides, and kept for one day to evaporate

the solvents at room conditions. The samples were then immersed in hot xylene for 10 min. Then they were taken out and put into iodine/acetone solution for 2 min. Finally they were washed out with acetone, and dried in vacuum (400 Torr) at room temperature. They were then coated with carbon. Magnification for all samples was set to 5000.

3.7 Calculation of the Characteristic Values, and the PVT Data of Polymers Using Group Contribution

While calculating the characteristic values, P^*, T^*, ρ^*, for polymers, one needs PVT data for each polymer and the empirical Tait equation is used for this purpose. This equation is capable for extrapolating data beyond the range of actual experiment within 0.001 cm^3/g which is better than the experimental error [79]. Tait equation is given as,

$$\upsilon(P,T) = \upsilon(0,T)\left\{1 - 0.0894 \ln\left[1 + \frac{P}{D(T)}\right]\right\} \tag{3.01}$$

where υ is specific volume (cm^3/g) at pressure P (MPa) and temperature T (K), whereas $\upsilon(0,T)$ is specific volume at zero pressure, and it is given by,

$$\upsilon(0,T) = V_o \exp(\alpha T) \tag{3.02}$$

or,

$$\upsilon(0,T) = V_1 + V_2 T + V_3 T^2 \tag{3.03}$$

where, α is thermal expansion coefficient, V_o, V_1, V_2, and V_3, are the coefficients. The parameter D (T) is usually given by an exponential function that describes the behavior of polymer under pressure. It is defined as,

$$D(T) = D_o \exp(mT) \qquad (3.04)$$

where m is a coefficient. To predict the PVT behavior of polymers by means of the Tait equation, group contribution modified cell model equation of state (GCMCM EOS) proposed by Sato et. al was utilized [80]. Their model using group contribution approach can predict the specific volume as a function of pressure and temperature with an average deviation as low as ±0.25%. Experimental observed values of specific volumes as a function of temperature and pressure are given in literature [81]. The standard deviations of percent difference between calculated from GCMCM EOS and experimental values (taken from [82]) of specific volume for Nylon 6 between 294.75-397.65 K are shown in Table 3.05. It is obvious that experimental and calculated values are consistent with each other with high correlation. At higher pressures, accuracy gets better.

Table 3.02 Standard percent deviations (SD%) between calculated and experimental values (taken from [[82]]) of specific volume for Nylon 6 between 294.75-397.65 K.

Pressure (MPa)		SD%
0		1.1
40		0.6
80		0.4
120		0.4
	Average	0.6

As mentioned earlier, *E-nBA-MAH* terpolymer contains ethylene, n-butyl acrylate, and maleic anhydrite groups with mole fractions 97.67%, 1.41% and 0.92%, respectively. The procedure used by Sato et. al. was applied to find out the PVT data of the *E-nBA-MAH* terpolymer. The results are shown in Fig. 3.05. Table 3.03 shows the Tait equation parameters for both polymers; it gives the specific volume as a function of pressure and temperature.
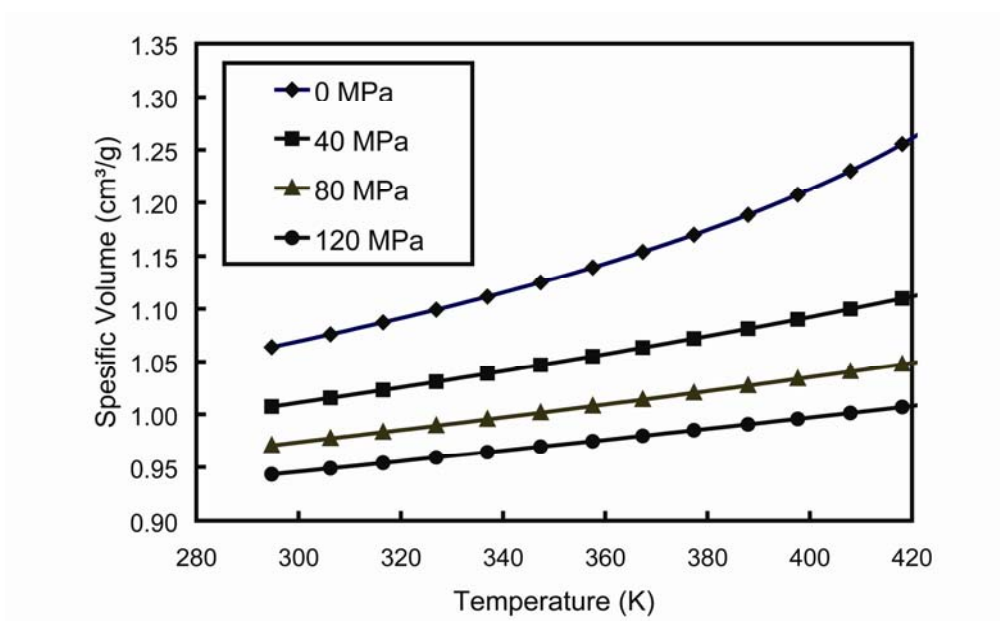
Figure 3.05 PVT data of the E-*n*BA-MAH terpolymer.

Table 3.03 Tait equation values for polymers.

Polymer	$V(0,T)\,(cm^3/g)$	$B(T)$ (MPa)
Nylon 6	$0.72\exp(6.80\times10^{-4}T)$	$165.57\exp(-4.2\times10^{-3}T)$
E-*n*BA-MAH	$1.43 - 3.19\times10^{-3}T + 6.62\times10^{-6}T^2$	$844\exp(-9.8\times10^{-3}T)$

The characteristic values used in SL EOS were found by fitting specific volume as a function of pressure and temperature for both polymers given by Eq. 2.06. The polymer used in the study was assumed to be a random terpolymer, and Eq. 2.07 was used to obtain the characteristic values for terpolymer. The results are listed in Table 3.04.

Table 3.04 Characteristic values for used polymers.

Polymer	P^* (MPa)	T^* (K)	ρ^* (g/cm^3)	υ^* (cm^3/g)	r (x10^4)
Nylon 6	468	567	1.226	10.073	0.110
E-nBA-MAH	38	627	0.996	134.331	0.025

3.8 Image Analysis of Nanofibers

Image analysis was performed by ImageJ software by measuring the diameters of nanofibers randomly from SEM images. Only one measurement was taken from each fiber. The scale of the image analyzer program was set to the scale of micrograph before the start of every measurement on the micrograph to make proper calibration.

3.9 Data Analysis of Nanofiber Distribution

The Johnson S_B probability density function y can be expressed as [63, 83, 84],

$$y = \frac{\delta}{\sqrt{2\pi}} \frac{(d_{max} - d_{min})}{(d - d_{min})(d_{max} - d)} \exp\left\{\left(-\frac{\delta^2}{2}\right)\left[\ln\left(\frac{d - d_{min}}{d_{max} - d}\right) - \ln\left(\frac{d_g - d_{min}}{d_{max} - d_g}\right)\right]^2\right\} \quad (3.05)$$

where, $d_{max} > d > d_{min}$ and d_{max}, d_{min}, and d are maximum observed, minimum observed, and observed diameters, respectively. δ is a parameter of distribution function giving the order of scattering, and d_g is geometric mean diameter of nanofibers. When the minimum, maximum, and geometric mean values are known a priori, maximum likelihood estimates the parameter $\hat{\delta} = 1/s_f$ [85] where,

$$s_f = \sqrt{\frac{1}{N}\sum_{i=1}^{N}\left[\ln\left(\frac{d - d_{min}}{d_{max} - d}\right) - \ln\left(\frac{d_g - d_{min}}{d_{max} - d_g}\right)\right]^2} \quad (3.06)$$

where N is observation number.

Letting,

$$\tau = \delta\left[\ln\left(\frac{d - d_{min}}{d_{max} - d}\right) - \ln\left(\frac{d_g - d_{min}}{d_{max} - d_g}\right)\right] \quad (3.07)$$

The cumulative distribution function becomes,

$$F(\xi) = \frac{1}{\sqrt{2\pi}}\int_{-\infty}^{\xi}\exp\left(-\frac{\tau^2}{2}\right)d\tau \quad (3.08)$$

27

This is a normal cumulative distribution function, where,

$$\xi = \delta \left[\ln \left(\frac{d - d_{min}}{d_{max} - d} \right) - \ln \left(\frac{d_g - d_{min}}{d_{max} - d_g} \right) \right]$$

(3.09)

As a result, the distribution can be represented by the parameters d_{max}, d_{min}, d_g, and δ. Then, the first and the second moments of the normalized diameter w can be estimated; w is given by,

$$w = \frac{d - d_{min}}{d_{max} - d_{min}}$$

(3.10)
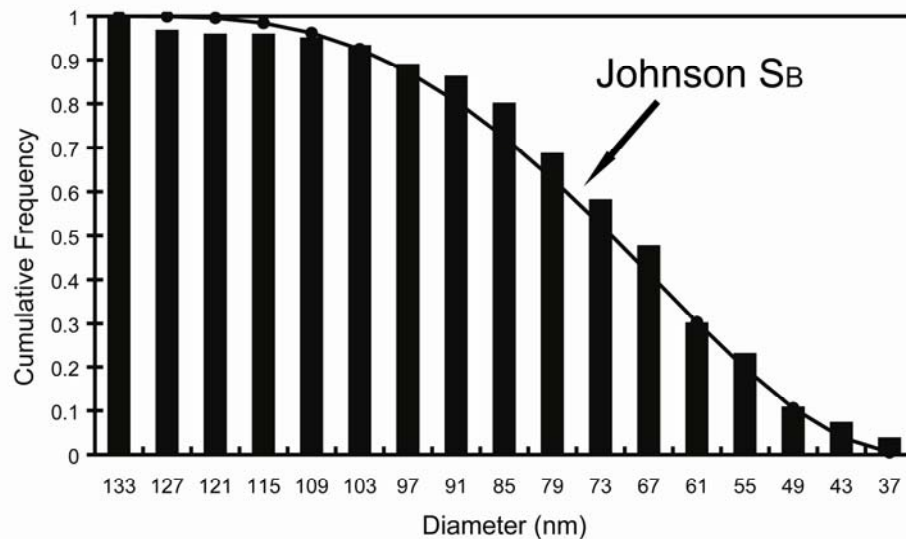
Figure 3.06 Cumulative frequency and calculated Johnson S_B distribution function of nanofibers obtained from 15% Nylon 6 /formic acid solution.

Johnson S_B distribution function gives consistent results with the observed values as seen in Fig. 3.06. The figure gives both observed

cumulative frequency of the diameters of nanofibers and calculated one from Johnson S$_B$ function.

Electrical field energy is proved to be responsible for the deformation mechanism of the droplet at the tip, and distribution of the nanofiber diameters in electrospinning process [86]. The electrical field energy (U) at total volume of nanofiber can be described as [87],

$$U = \int_V \frac{1}{2} \varepsilon |\vec{E}|^2 \, dV \tag{3.11}$$

where, ε is permittivity of nanofiber solution system. If one assumes the nanofiber to be in cylindrical shape (d the diameter of nanofiber and l the length of fiber) and system consists of homogenous nanofiber material, then the volume of the system (V) is simply,

$$V = \frac{\pi d^2}{4} l \tag{3.12}$$

Then one can write,

$$\frac{dV}{V} = 2\frac{dd}{d} + \frac{dl}{l} \tag{3.13}$$

The substitution Eq 3.13 in Eq 3.11 and its evaluation yields,

$$U = V\varepsilon |\vec{E}|^2 \left(\ln d_f - \ln d_i + \frac{1}{2} \ln \frac{l_f}{l_i} \right) \tag{3.14}$$

where, d_i and d_f are initial and final diameters of nanofiber, respectively. l_f/l_i is the ratio of final length of the nanofiber to its initial length. The value of $\ln(l_f/l_i)$ is greater then zero and becomes a large value (φ) for a produced fiber. Also, the volume can be expressed as,

$$V = Qt \tag{3.15}$$

where Q is constant feed rate of the system, and t is processing time. Eq 3.14 turns out to be,

$$U = Qt\varepsilon\left|\vec{E}\right|^2\left(\ln d_f - \ln d_i + \varphi\right) \tag{3.16}$$

The electrical field, $\vec{E}$, can be taken to be approximately equal to the external electrical field $\vec{E}_\infty$, and given as a function of distance along z-direction [88],

$$E(z) \cong E_\infty(z) = \frac{\phi}{\left(\dfrac{d_i}{4} + z - \dfrac{z^2}{2L}\right)\ln\left(1 + \dfrac{8L}{d_i}\right)} \tag{3.17}$$

where, ϕ is electrical potential, L is distance between tip and collector. Substituting Eq. 3.17 in Eq 3.16 yields,

$$U = Qt\varepsilon\,\frac{\phi^2}{\left(\dfrac{d_i}{4} + z - \dfrac{z^2}{2L}\right)^2\ln^2\left(1 + \dfrac{8L}{d_i}\right)}\left(\ln d_f - \ln d_i + \varphi\right) \tag{3.18}$$

The power of the deformation energy (P) can be defined as the energy of deformation per unit time. It reads as follows,

$$P(t) = Q(t)\varepsilon(t)\frac{\phi^2}{\left(\dfrac{d_i}{4} + z(t) - \dfrac{z^2(t)}{2L}\right)^2 \ln^2\left(1 + \dfrac{8L}{d_i}\right)}\left(\ln d_f(t) - \ln d_i + \varphi(t)\right) \qquad (3.19)$$

The parameters are function of time due to evaporation of solvent, time of travel of polymeric jet, and thinning of the jet.

The $\ln d_f$ term can be Taylor expanded,

$$\ln d_f = \sum_{n=1}^{\infty} \frac{(-1)^{n+1}}{n}(d_f - 1)^n \qquad (3.20)$$

Taking the first two elements makes Eq. 3.19 as,

$$\ln d_f \cong -0.5 d_f^{\,2} + 2 d_f - 1.5 \qquad (3.21)$$

The expected value $\langle d_f \rangle$ for the final diameter of fibers can be given as [87],

$$\ln\langle d_f \rangle \cong -0.5\langle d_f^{\,2} \rangle + 2\langle d_f \rangle - 1.5 \qquad (3.22)$$

where, $\langle d_f \rangle$ is the first moment, and $\langle d_f^{\,2} \rangle$ is the second moment of the distribution of diameters of observed nanofibers. Substituting Eq 3.22 into Eq. 3.19, and letting $z = L$ yields,

$$P(t) = Q(t)\varepsilon(t)\frac{\phi^2}{\chi}\left(\ln < d_f > - \ln d_i + \varphi(t)\right) \qquad (3.23)$$

where,

$$\chi = \left(\frac{d_i}{4} + \frac{L}{2}\right)^2 \ln^2\left(1 + \frac{8L}{d_i}\right)$$

<div align="right">(3.24)</div>

The power required for deformation depends on electrospinning process parameters as given by Eq. 3.23. However, it was demonstrated and verified by many researchers that allometric scaling approximation gives also good correlation between normalized process parameters and final diameter of the electrospun nanofibers as done in this study [89].

3.10 Atomic Force Microscopy (AFM)

Force-deflection data are acquired from Atomic Force Microscopy (Park System, XE-100, probe, ContDLC). Force and distance limits are set to 2.5 nN, and ±1.25 µm, respectively. The probe is spherical monolithic silicon and has symmetric tip shape with chip size 3.4 x 1.6 x 0.3 mm. The tip side of the cantilever is coated with diamond-like carbon with 15nm thickness, and the detector side of the cantilever is coated with aluminum 30 nm thick. AFM tip properties are given in Table 3.05.

Table 3.05 Properties of AFM tip.

Property	
Resonance Frequency	13 kHz
Force Constant	0.2 N/m
Length	450 µm
Mean Width	50 µm
Thickness	2 µm
Tip Height	17 µm
Tip Radius	< 15 nm

3.10.1 Data Acquisition of AFM

A typical AFM image is shown in Fig. 3.07. The detection procedure of acquiring of force-deflection data is as follows; the AFM tip touches at nanofiber and moves along the axial direction at a rate of 1 µm /s The fiber is stationed on glass substrate. However, Z-scan detector signal develops non-linearity and noise (Fig. 3.08); and therefore Z-fit detector data are filtered according to the calibration of laser detector (Fig. 3.09). Z-fit detector data give more accurate information then that of Z-detector raw data [90]. Fig. 3.07 shows the force-height of AFM probe laser deflection coming from Z-scan detector, while Fig. 3.09 shows maximum and minimum force and height values for neat Nylon 6.
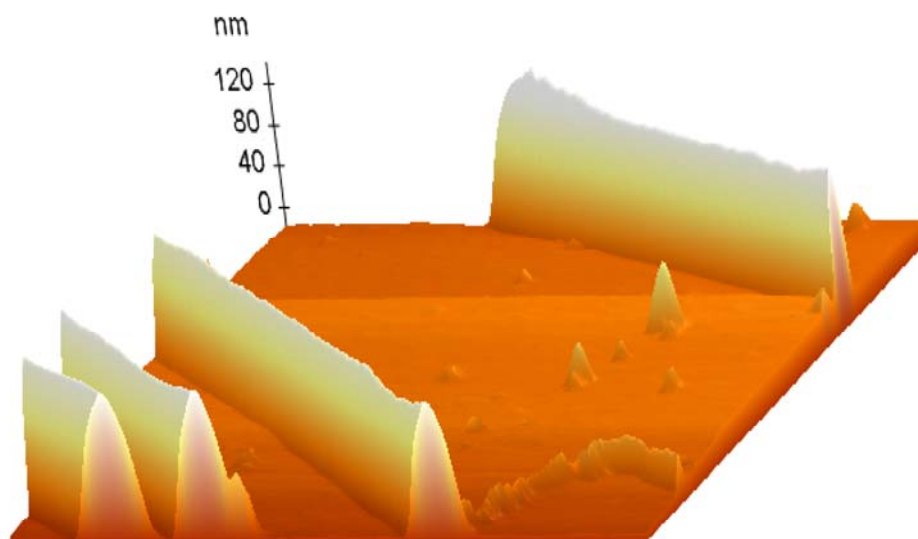
Figure 3.07 AFM image of nanofibers.
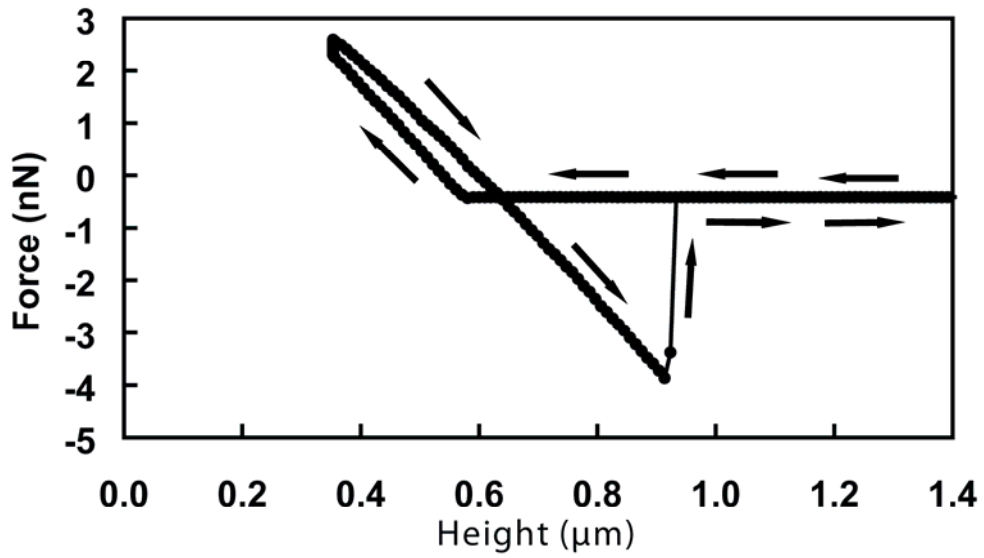
Figure 3.08 Z- detector signal for Force (nN) and height of cantilever (nm).
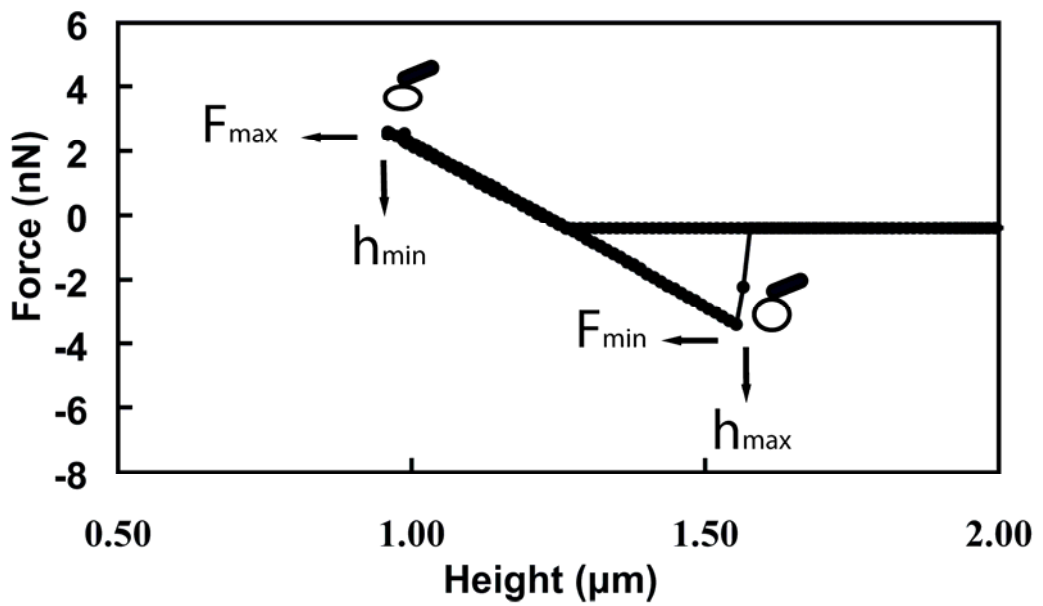
Figure 3.09 Z- fit signal for max. and min. Forces (nN) and max and min heights of cantilever (nm) and corresponding deformation of the nanofiber.

3.10.2 Data Analysis of AFM

Force is defined as,

$$F = k_c(h_c - h_{c\min})$$
(3.24)

wherein, k_c is the spring constant of cantilever given in Table 3.05 and h_c is cantilever height and $h_{c\mathit{min}}$ is the minimum height of cantilever. The Hertz theory gives the relation of force (F) for the indentation of a linear elastic, infinite half- rigid sphere tip in contact [73, 91],

$$F = \frac{4ER^{1/2}\delta^{3/2}}{3(1-\nu^2)}$$
(3.25)

where E is elastic modulus of material, R is radius of tip, δ is indentation depth and ν is Poisson's ratio. The raw data taken from AFM are transformed into indentation (δ) according to cantilever deflection h_c and base displacement h_z,

$$\delta = (h_z - h_{z\min}) - (h_c - h_{c\min})$$
(3.26)

where, $h_{z\mathit{min}}$ is height of base which corresponds to minimum cantilever height $h_{c\mathit{min}}$ maximum force (Fig.3.10).

Material being deformed is modeled according to combined Maxwell-Kelvin-Voigt material model with spring and dashpot elements as given in Fig. 3.11.
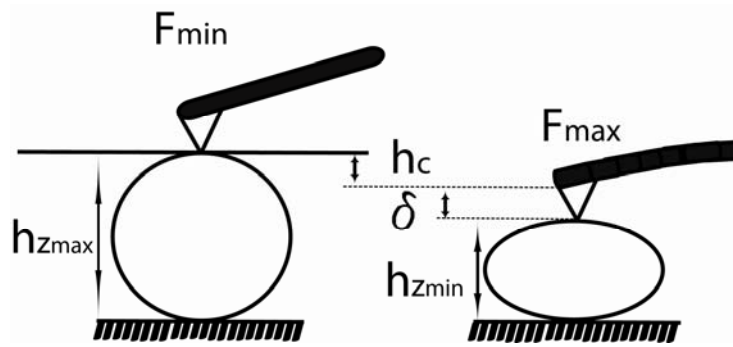
Figure 3.10 Deformation of nanofiber under AFM probe.
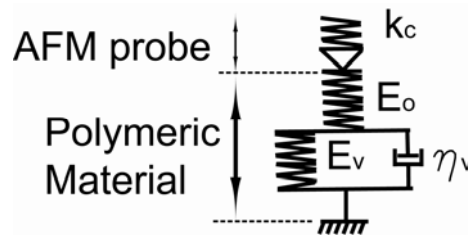
Figure 3.11 Combined Maxwell-Kelvin-Voigt material model with spring and dashpot elements model for polymeric material and AFM probe.

Vandamme and Ulm gives force response of the Maxwell-Kelvin-Voigt material which contains both creep and relaxation phenomena as [77],

$$F(t) = 4 + \frac{E_{eff}}{E_v}\left[1 - \exp\left(\frac{-E_v t}{\eta_v}\right)\right] + \frac{E_{eff}(1-2v_o)^2}{E_o + 3E_v}\left[1 - \exp\left(-\frac{E_o + 3E_v t}{3\eta_v}\right)\right] \quad (3.27)$$

where, E_v and E_o are elastic moduli of material (Fig. 3.09), η_v is viscous modulus, v_o Poisson's ratio, t is time. E_{eff} is effective elastic modulus of the system and defined if elastic modulus of cantilever is higher than that of material being deformed,

$$E_{eff} \cong \frac{E}{(1-\nu^2)}$$ (3.28)

The substitution of Eq. 3.27 and Eq. 3.28 into Eq 3.25 and taking the Poisson's ratio of material to be $\nu_o \cong 0.5$ yields [73, 77],

$$\delta^{3/2} = \frac{3(1-\nu^2)}{ER^{1/2}} + \frac{3}{4R^{1/2}E_v}\left[1 - \exp\left(\frac{-E_v t}{\eta_v}\right)\right]$$ (3.29)

Rearranging Eq. 3.29 results in,

$$\delta^{3/2} = A(t).\exp(-\psi t)$$ (3.30)

where

$$A(t) = \left[\frac{3(1-\nu^2)}{ER^{1/2}} + \frac{3}{4R^{1/2}E_v}\right]\exp\left(\frac{E_v t}{\eta_v}\right) - \frac{3}{4R^{1/2}E_v}$$ (3.31)

and

$$\psi = \frac{E_v}{\eta_v} = \frac{1}{\tau_o}$$ (3.32)

where, τ_o, is relaxation time and defined as the time needed the polymer chain configurations into the unperturbed state.

Taking the logarithm of Eq.3.30 gives,

$$1.5\ln\delta = -\psi t + \ln A(t)$$ (3.33)

Eq. 3.33 has $\ln A(t)$ term which is non-linear part of this function, and for a certain time interval '$1.5\ln\delta$' vs. 't' graph gives linear line as seen from Fig. 3.12. Its slope is equal to ψ which is given in Eq. 3.32. For

convenience, linear portion of curve is taken in certain time interval till the point where F=0.
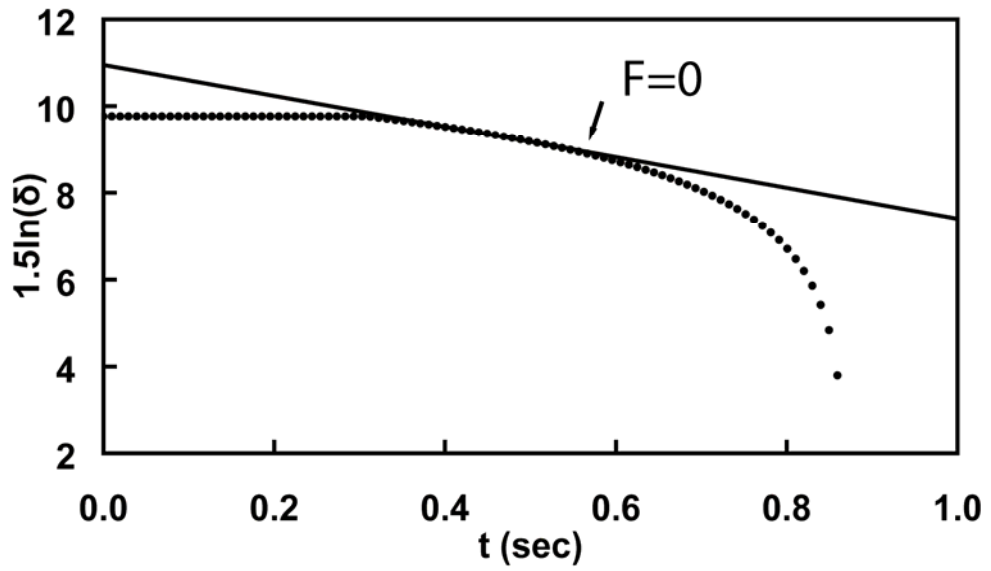
Figure 3.12 $1.5\ln\delta$ vs. t graph for the deformation of single nanofiber.

CHAPTER 4

RESULTS AND DISCUSSION

This chapter gives results of the works and related discussions.

4.1 WAXS Spectrum of Nanofibers

The characteristic peaks of the α phase at room temperature in the X-ray diffraction pattern of Nylon 6 are around $2\theta=20^{o}$ and 23.7°, and are indexed as (200) and (002)/(202) reflections, respectively.
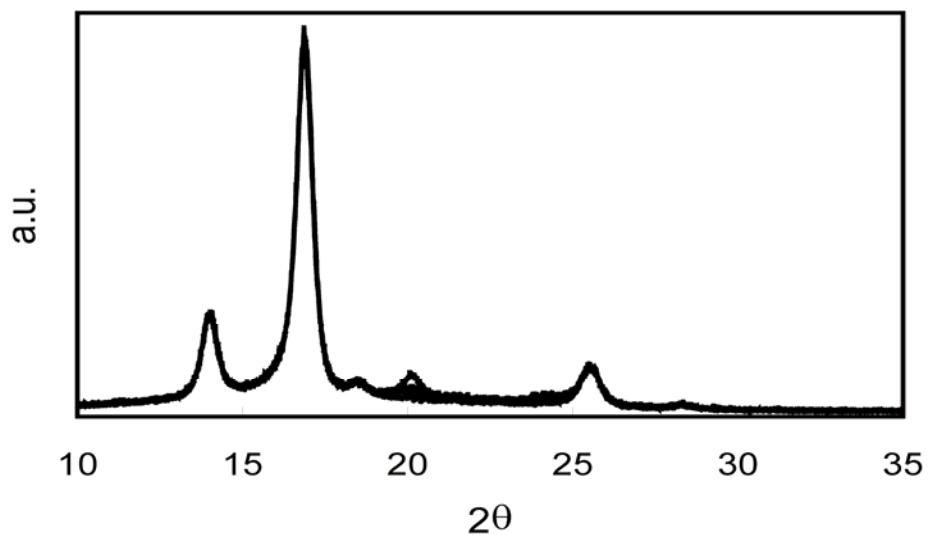
Figure 4.01 WAXS patterns of four different blends.

For the γ phase, the diffraction peaks around 2θ=10.7 and 21.4° are indexed as (020) and (001), respectively [53]. As seen in Fig. 4.02, the remarkable change of the WAXS spectrum, given in Fig. 4.01, occurs at the band of α phase at the vicinity of 20° and 23.7°. The sample that has 5% *E-nBA-MAH* terpolymer gives more intensity than others.

Annealing effect could be observed in Fig. 4.01, as well. It is clearly seen that heat assists the formation of crystals. The kinetics of formation of crystals is presented in Section 4.3. The enlarged portion of the diffraction pattern having variations is given in Fig. 4.02.
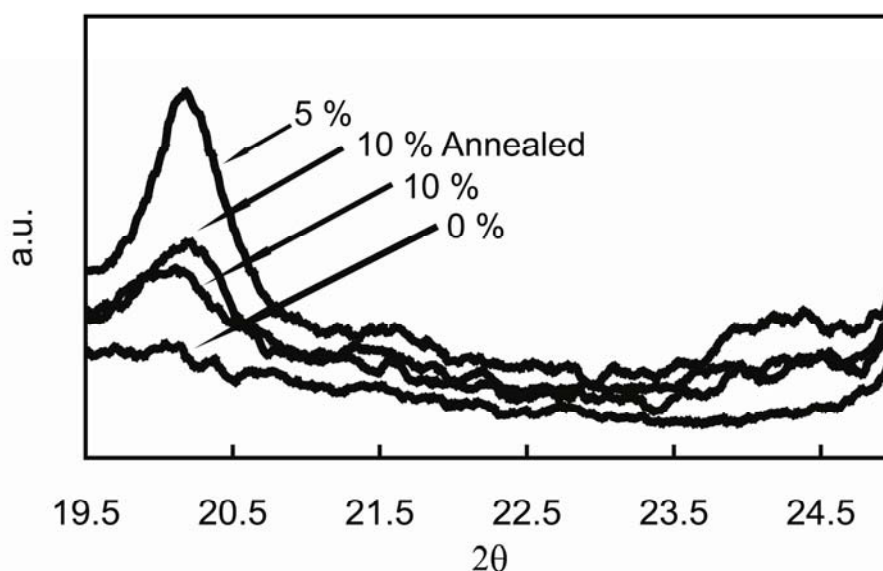
Figure 4.02 WAXS tracks of blends between 19.5° and 25°.

4.2 Melting Point Depression Analysis

The melting point depression method is used to find out the equilibrium melting point of many large crystals. Nylons exhibit polymorphism and give multiple peaks in their DSC traces as seen in Fig. 4.03. These peaks mainly refer to the melting of the crystals with different crystal

perfection. Peak I is ascribed to the boundary microcrystalline structures between the larger crystals, and Peak III corresponds to the melting of the crystalline sites with the highest perfection [57]. Analysis is performed for Peak II to get further information about the main crystals responsible for the formation of crystal sites in the polymeric blends.
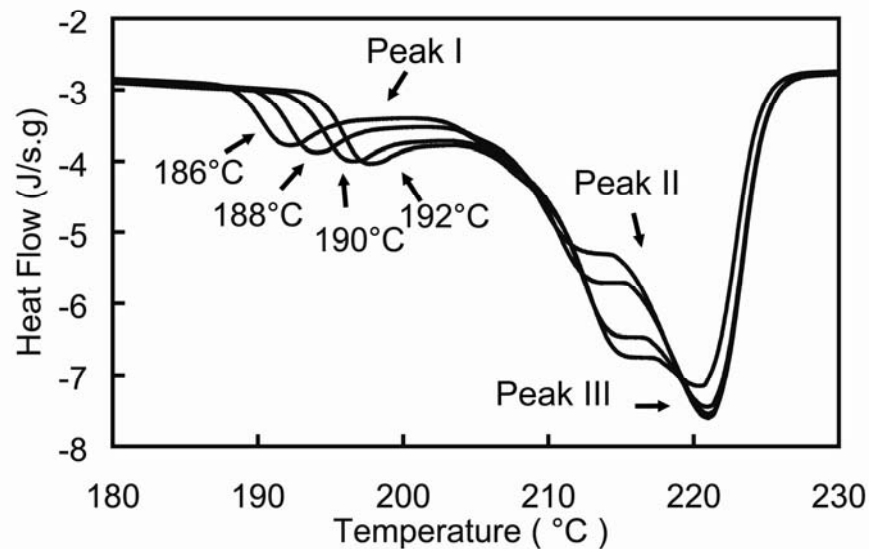
Figure 4.03 DSC traces for neat Nylon 6 at various crystallization temperatures.

Hoffman and Weeks (HW) [92] technique is used to find the equilibrium melting point of the blends. In this procedure, the equilibrium melting point of many large crystals is estimated by extrapolating the observed melting points (T_m) of the samples crystallized (i.e. with finite crystal dimensions) isothermally at temperature T_c to the $T_m=T_c$ line. Fig. 4.04 shows HW plots. The intersection of the linear line for various crystallization temperatures and the diagonal (45°) line gives the equilibrium melting temperature.
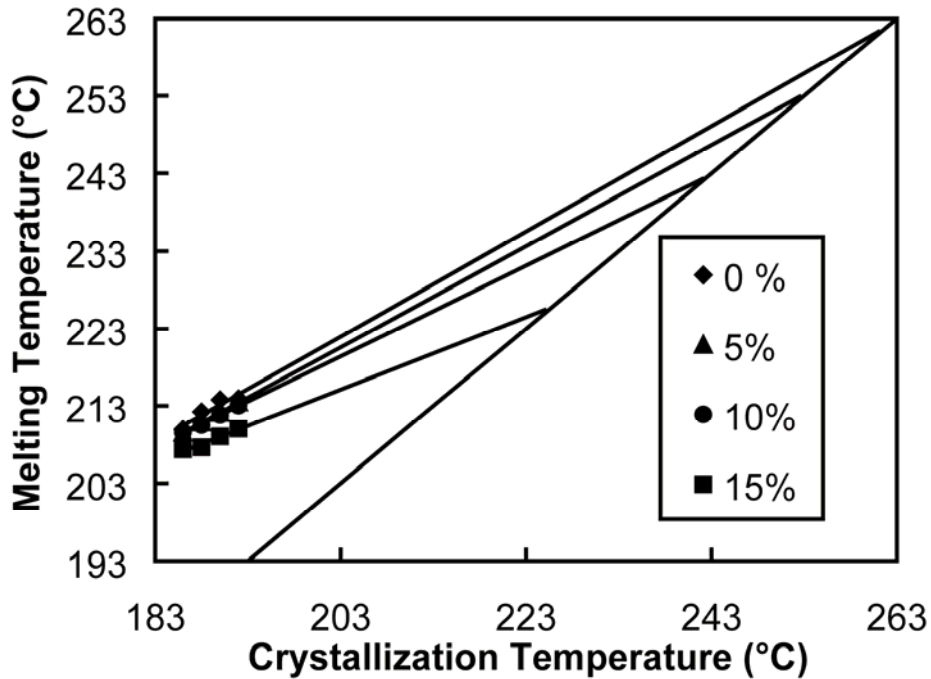
Figure 4.04 Hoffman-Weeks plots for Nylon 6/E-*n*BA-MAH blends at various contents.

4.2.1 Interaction Energy by FH Approach Based on Melting Point Depression

Fig. 4.05 shows the equilibrium melting point depression of Nylon 6/E-*n*BA-MAH blends as a function of $(1-\phi_2)^2$ given in Eq.2.05. The equation implies that the slope of the linear line gives $B_{12}T_m^o/\Delta h_{2u}$ term. The interaction energy between Nylon 6/E-*n*BA-MAH is determined from the slope of straight line in Fig. 4.04 by using Δh_{2u} =166.46 MPa in Eq. 2.04. The interaction energy per unit volume is then found to be B_{12}=-721.56 MPa. The negative value means, the polymer pair is thermodynamically favorable when mixed together at all compositions and temperature [93].

42
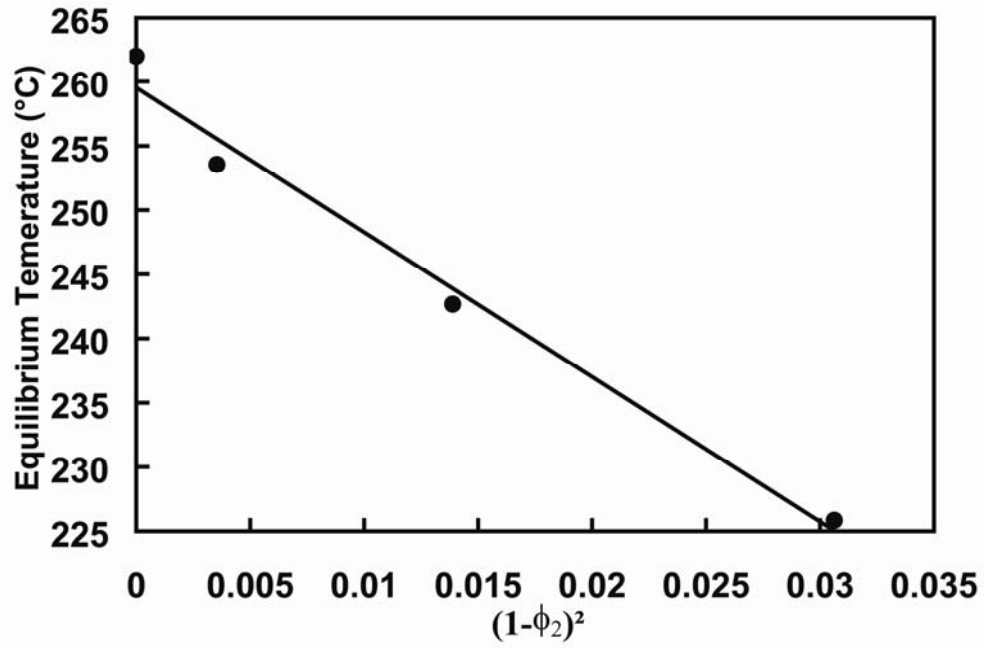
Figure 4.05 Interaction energy of Nylon 6/E-nBA-MAH
pairs according to Flory-Huggins Theory.

4.2.2 Interaction Energy by SL-EOS Approach Based on Melting Point Depression

The bare interaction energy, ΔP^*, which is equivalent of B_{12} in FH theory can be determined from melting point data by rearranging Eq. 2.08 as follows,

$$\Delta P^*(1-\phi_2)^2 = -\frac{\Delta h_{2u}}{\tilde{\rho}}\left(1-\frac{T_{mb}^o}{T_m^o}\right)$$
$$-\frac{RT_{mb}^o}{\tilde{\rho}}\left(\frac{1}{r_2^o v_2^*}-\frac{1}{rv^*}\right)-\frac{RT_{mb}^o}{\tilde{\rho}r_2^o v_2^*}\ln\left(\frac{\tilde{\rho}\phi_2}{\tilde{\rho}_2}\right) \qquad (4.01)$$
$$-\frac{RT_{mb}^o}{\tilde{\rho}v_2^*}\left(\frac{(1-\tilde{\rho})\ln(1-\tilde{\rho})}{\tilde{\rho}}-\frac{(1-\tilde{\rho}_2)\ln(1-\tilde{\rho}_2)}{\tilde{\rho}_2}\right)$$

The bare interaction energy can be evaluated from the slope of a plot of the RHS terms of Eq. 4.01 vs. the square of the second components' volume fraction $(1-\phi_2)^2$ (Fig. 4.06). The interaction energy per unit volume calculated from the slope is $B_{12}=-410.15$ MPa. This number is 43% lower than the one obtained from FH theory. However, SL EOS theory gives results more accurate than FH theory.
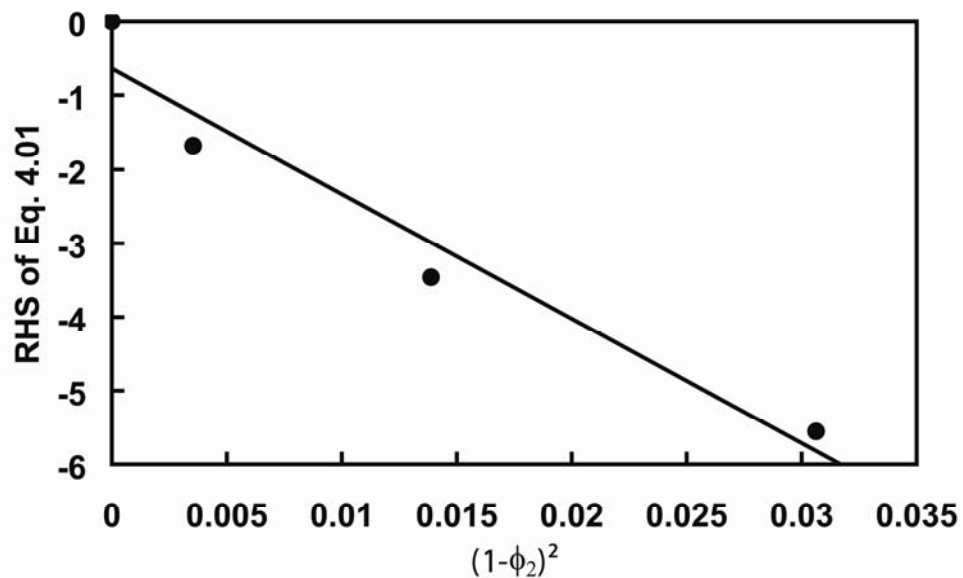
Figure 4.06 Interaction Energy of Nylon 6 / E-*n*BA-MAH
pairs according to SL EOS.

4.3 Isothermal Crystallization Analysis

The information about the extent of crystallization of polymers as a function of the time can be obtained from DSC patterns. Figure 4.07 gives the change of percent crystallinity in time for different blends at the crystallization temperature of 192°C. All the data at the crystallization temperatures of 186, 188, 190 and 192 ^{o}C have been collected.
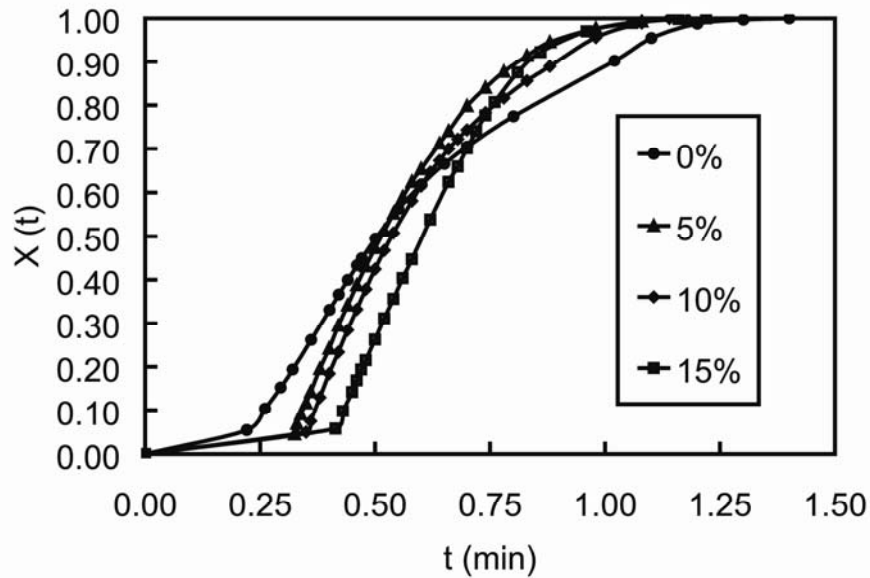
Figure 4.07 Percent crystallization of blends in time at crystallization temperature of 192°C.

The data for all crystallization temperatures were plotted on log-log scale to get the Avrami parameters from Eq. 2.16. Figure 4.08 depicts the sample plot for the crystallization temperature of 192 $^{\circ}$C. It is seen that all crystallization processes can be divided into 4 individual stages, which are named from the beginning to the end as initiation, post-initiation, propagation, and termination stages. These stages are determined by the straight line portions of the curves. The upper and lower limits of the stages of the polymers determined from the plots are listed in Table 4.01.
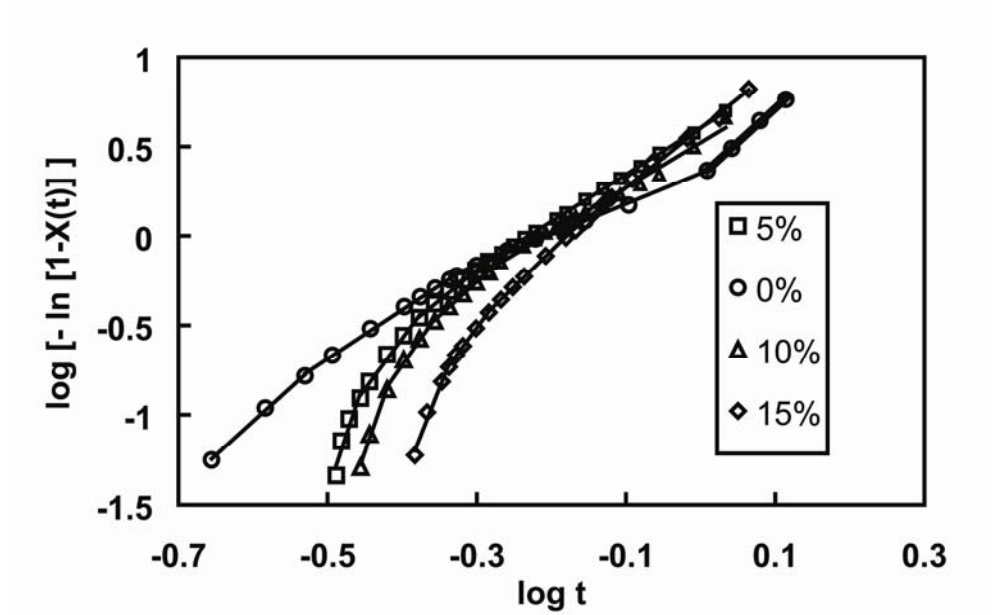
Figure 4.08 $\log\{\ln[1-X(t)]\}$ vs $\log t$ graph of blends at crystallization temperature of 192°C.

Table 4.01 Weight fractions of crystallized polymer material X(t).upper and lower limits at various phases of the crystallization processes of blends.

Blend Composition (w/w)	Weight Fraction X(t) (%)			
N6 / E-nBA-MAH	Initiation	Post-initiation	Propagation	Termination
100/0	5-17	17-40	40-90	90-99
95/5	5-12	12-30	30-51	51-99
90/10	5-13	13-28	28-47	47-99
85/15	5-17	17-31	31-63	63-99

Tables 4.02-4.05 list the Avrami parameters of the blends for the crystallization stages of initiation, post-initiation, propagation, and termination, at various crystallization temperatures, respectively.

46

Avrami parameter 'n' gives the information about the type of crystallization process [47]. Nylon 6 has initially increasing spherulitic nucleation rate as seen in Tables 4.02 and 4.03. Then, polymorphic transformation rate stops increasing, and decreases throughout remaining time. In propagation it demonstrates mostly fibril-like and disk-like random growth from grain edges after saturation. It implies that there is a change of growth mechanism (Table 4.04). At the end of crystallization, transformation completes with increasing diffusion controlled growth as implied in Table 4.05. Generally, *E-nBA-MAH* terpolymer addition accelerates the polymorphic transformation, and then slows randomly down at all sites. The main difference of transformation mechanism between neat Nylon 6 and blended ones is that the terpolymer does not permit the system to decelerate for saturation; but transformation keeps going at all sites at low rate. The increase of temperature accelerates transformation as expected.

Table 4.02 Avrami parameters for isothermal crystallization of polymers at initiation stage of crystallization at various crystallization temperatures.

$T_c(^oC)$	0%			5%			10%			15%		
	n	K (min^{-1})	R^2	n	K (min^{-1})	R^2	n	K (min^{-1})	R^2	n	K (min^{-1})	R^2
186	3.09	6.07	0.99	12.23	2088.3	0.99	4.18	7.31	0.99	6.44	31.75	0.99
188	4.21	11.89	0.99	14.31	15678.3	0.98	10.25	1105.61	0.99	8.85	121.56	0.99
190	3.96	17.69	0.99	14.19	48161.5	0.98	9.50	3566.97	0.98	9.45	205.49	0.99
192	3.76	16.53	0.99	13.50	189889.1	0.95	11.96	15045.27	0.99	1.27	1280.56	0.99

Table 4.03 Avrami parameters for isothermal crystallization of polymers at post-initiation stage of crystallization at various crystallization temperatures

$T_c(^oC)$	0%			5%			10%			15%		
	n	K (min^{-1})	R^2	n	K (min^{-1})	R^2	n	K (min^{-1})	R^2	n	K (min^{-1})	R^2
186	3.29	7.65	0.98	7.51	49.87	0.99	4.45	9.38	0.99	5.63	16.61	0.99
188	3.33	5.09	0.99	8.23	109.27	0.99	6.22	32.60	0.99	6.314	19.15	0.99
190	2.95	5.51	0.99	6.55	48.61	0.99	5.19	35.21	0.99	6.993	32.30	0.98
192	3.76	16.53	0.99	13.50	189889.1	0.99	11.96	15045.27	0.99	11.26	1280.6	0.99

The rate parameter K increases with increasing crystallization temperature at initiation and post-initiation stages (Tables 4.2 and 4.3). Later stages of the crystallization have decreasing crystallization rate at increasing crystallization temperature as seen in Table 4.04 and 4.05. Also, crystallization rate parameter of initial stage is higher than later stages of the crystallization process. The already formed crystallization sites of the system lower the rate of the process. The addition of 5% *E-nBA-MAH* into Nylon 6 increases the rate more than the other compositions.

Table 4.06 gives the Avrami crystallization kinetics parameters. Generally, during the whole crystallization process, Nylon 6 shows diffusion controlled crystallization with decreasing rate forming random shapes. *E-nBA-MAH* elastomer blending accelerates the crystallization, but after nucleation the nucleus grows with decreasing rate except the neat Nylon 6 and the blend with 5% *E-nBA-MAH* terpolymer. The same trend can be observed in Table 4.07 which gives the kinetic parameters t_{max}, $t_{1/2}$, and G given by Eq. 2.12, 2.13, and 2.14, respectively.

Activation energy of crystallization is calculated from the slope of the plot of Eq. 2.16. In order to compare the magnitude of the released energy during crystallization all negative values were converted into positive values. Figure 4.09 shows all stages of crystallization process with increasing *E-nBA-MAH* elastomeric terpolymer content. It is observed that initiation stage of the crystallization (e.g. nucleation) generally requires more energy than other stages regardless of the blend composition. While the crystallization process proceeds, energy requirement of the system tends to decrease. The desired energy for initiation of crystallization gradually increases with *E-nBA-MAH* content. Nevertheless, after 10% addition of *E-nBA-MAH,* the required energy for nucleation drops down drastically. It is easy to have nucleation after 10% addition of *E-nBA-MAH*.

Table 4.04 Avrami parameters for isothermal crystallization of polymers at propagation stage of crystallization at various crystallization temperatures

T_c(°C)	0%			5%			10%			15%		
	n	K (min^{-1})	R^2	n	K (min^{-1})	R^2	n	K (min^{-1})	R^2	n	K (min^{-1})	R^2
186	1.73	2.31	0.99	5.43	12.61	0.99	4.11	7.29	0.99	4.90	10.15	0.99
188	1.91	2.14	0.99	5.32	14.10	0.99	4.41	8.48	0.99	5.28	10.02	0.99
190	1.66	2.20	0.99	4.17	8.16	0.99	3.55	8.03	0.99	4.30	5.88	0.99
192	1.71	2.24	0.99	3.38	6.64	0.99	3.80	7.64	0.99	4.03	5.28	0.99

Table 4.05 Avrami parameters for isothermal crystallization of polymers at termination phase of crystallization at various crystallization temperatures

T_c(°C)	0%			5%			10%			15%		
	n	K (min^{-1})	R^2	n	K (min^{-1})	R^2	n	K (min^{-1})	R^2	n	K (min^{-1})	R^2
186	3.78	2.24	0.99	3.03	3.91	0.98	3.14	4.20	0.99	3.53	5.69	0.99
188	4.12	1.93	0.99	6.41	13.52	0.98	2.84	3.50	0.99	3.55	5.08	0.98
190	3.60	2.10	0.99	2.90	4.07	0.99	2.40	3.67	0.99	3.92	5.27	0.99
192	3.81	2.15	0.99	2.62	4.03	0.99	2.51	3.33	0.99	3.32	4.01	0.99
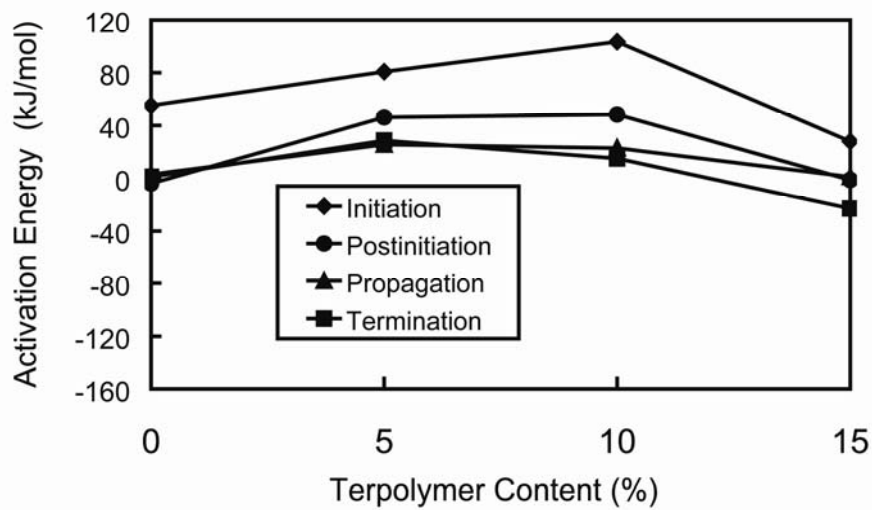
Figure 4.09 Activation energies of blends at various compositions at various crystallization stages.

Fig. 4.10 depicts the percent crystallinity values of the blends at various crystallization temperatures calculated from Eq. 2.11. The butyl acrylate group of *E-nBA-MAH* terpolymer reduces the crystallinity. The terpolymer interacts more strongly with Nylon 6 at 5% composition. Hence crystallinity decreases at 5% *E-nBA-MAH* content. But after 5% addition crystallinity goes up to the original level which is the percent crystallinity of Nylon 6.
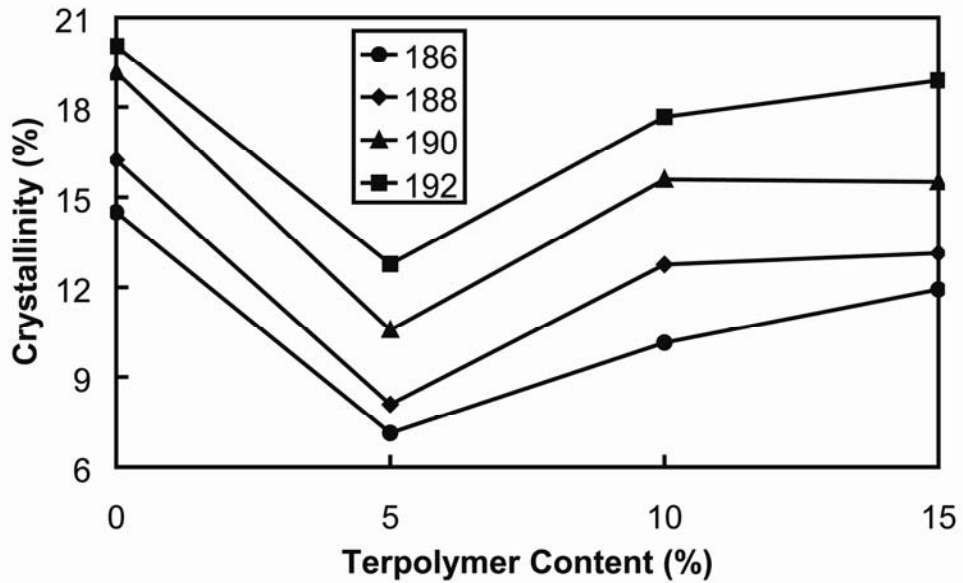
Figure 4.10 Percent crystallinity of the blends at various
crystallization temperatures.

Crystallinity of polymers is affected by the capability of the mobility of
polymer chains. Temperature helps the polymer system to come to their
individual configuration states as observed in Fig.4.09. Neat Nylon 6 has
high crystallinity compared to blends. However, the crystallinity with
increasing terpolymer content increases to the level of neat Nylon 6 due to
the heterogeneous regions of terpolymer in the system. High contents of
terpolymer causes aggregation yielding heterogeneous segregation and
Nylon 6 phase can crystallize more efficiently.

The activation energy needed for each blend is given in Fig. 4.11. The
addition of the elastomeric terpolymer decreases the activation energy. The
polymer with 5% elastomer content needs more energy than others. It can be
concluded that the addition of 5% terpolymer into Nylon 6 inhibits
crystallization much more than others. This effect loses its strength by
increasing the blending content due to strong secondary forces of Nylon 6 as
mentioned earlier.

Table 4.06 Avrami parameters for isothermal crystallization of polymers

T_c(°C)	0%			5%			10%			15%		
	n	K (min^{-1})	R^2	n	K (min^{-1})	R^2	n	K (min^{-1})	R^2	n	K (min^{-1})	R^2
186	2.38	2.86	0.98	4.57	5.96	0.93	3.56	4.65	0.99	4.56	7.46	0.98
188	2.67	2.62	0.97	5.98	13.99	0.97	3.80	4.41	0.95	4.90	7.13	0.97
190	2.29	2.76	0.98	3.90	5.15	0.95	3.34	5.02	0.95	4.91	6.92	0.97
192	2.34	2.93	0.98	3.47	5.40	0.95	3.42	4.45	0.93	4.16	4.76	0.97

Table 4.07 Kinetic parameters of (t_{max}, $t_{1/2}$, and G) for isothermal crystallization of polymers

T_c(°C)	0%			5%			10%			15%		
	t_{max} (min)	$t_{1/2}$ (min)	G (min^{-1})	t_{max} (min)	$t_{1/2}$ (min)	G (min^{-1})	t_{max} (min)	$t_{1/2}$ (min)	G (min^{-1})	t_{max} (min)	$t_{1/2}$ (min)	G (min^{-1})
186	0.51	0.55	1.82	0.64	0.62	1.60	0.59	0.59	1.71	0.61	0.59	1.68
188	0.58	0.61	1.65	0.62	0.60	1.65	0.62	0.61	1.63	0.64	0.62	1.62
190	0.51	0.56	1.79	0.61	0.60	1.67	0.55	0.55	1.81	0.64	0.63	1.60
192	0.49	0.54	1.86	0.56	0.55	1.81	0.58	0.58	1.72	0.64	0.63	1.59
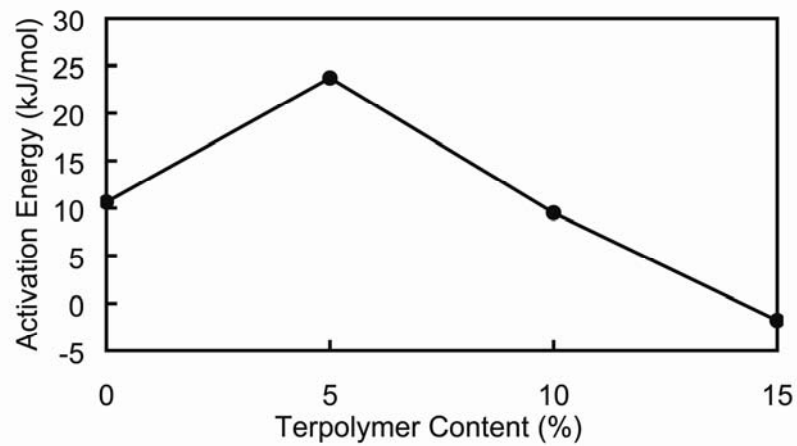
Figure 4.11 Activation of crystallization of blends during
the whole crystallization process.

The same tendency can be observed in Fig.4.12, which gives the numerical values of the constants A and B of Eq. 2.20. A is a constant related to the preexponential constant of spherulitic growth and B is a constant related to the energy of formation of the spherulitic growth from nucleus. The constant A increases rapidly with the addition of 5% *E-nBA-MAH*, but drops down to a value greater than that of neat Nylon 6. The constant B increases first up to 5% *E-nBA-MAH* addition. However it drops down again with continuing addition of terpolymer into Nylon 6.
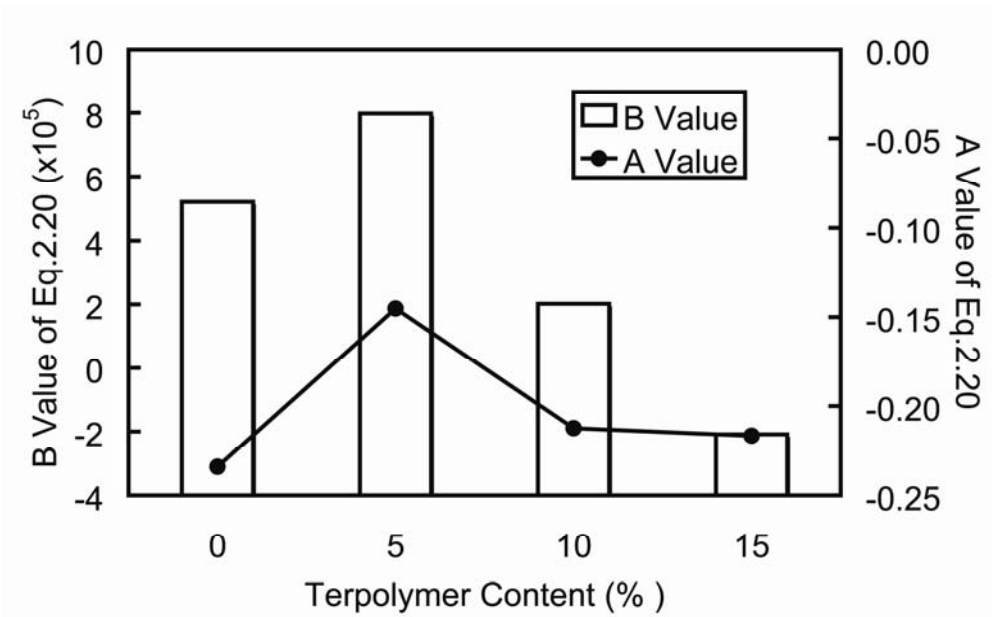
Figure 4.12 A and B values of Eq. 2.20.

4.4 Morphology of Blends

SEM micrograph of neat Nylon 6 is shown in Fig. 4.13. The regions seen in Fig. 4.14 as holes are the spaces left by elastomer which was dissolved away by hot xylene. As the elastomer content increases the holes generated also increases as seen in Fig. 4.15.

4.5 Effect of Elastomer on Nanofibers

Table 4.08 gives the parameters of the distribution the observation number (N), the maximum observed diameter (d_{max}), the minimum observed diameter (d_{min}), and the geometric mean of the diameters (d_g) of the nanofibers obtained from Nylon 6 and *E-nBA-MAH* elastomeric terpolymer electrospun at 15 kV and 10 cm tip-to-collector distance.
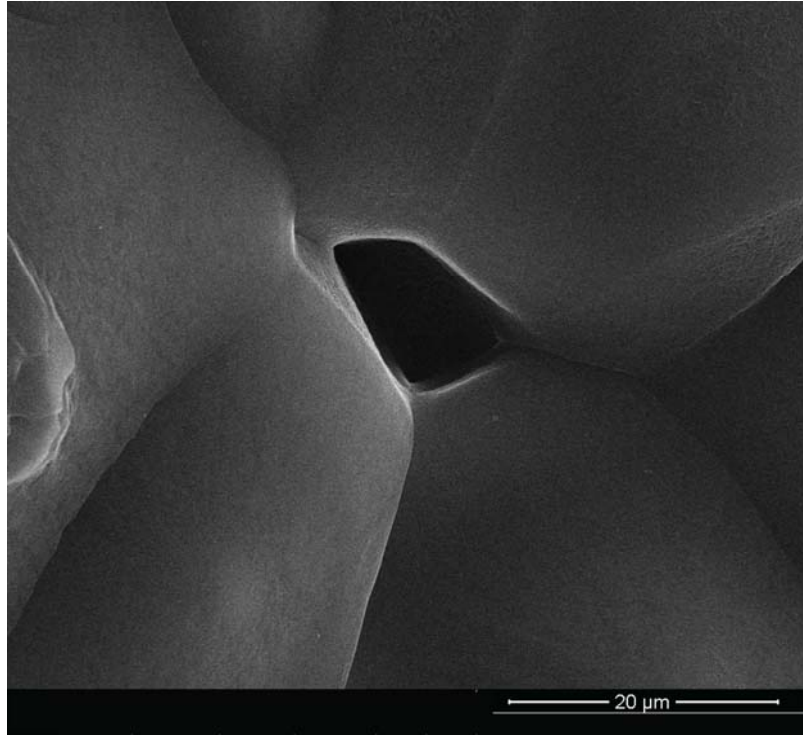
Figure 4.13 Neat Nylon 6 SEM image.
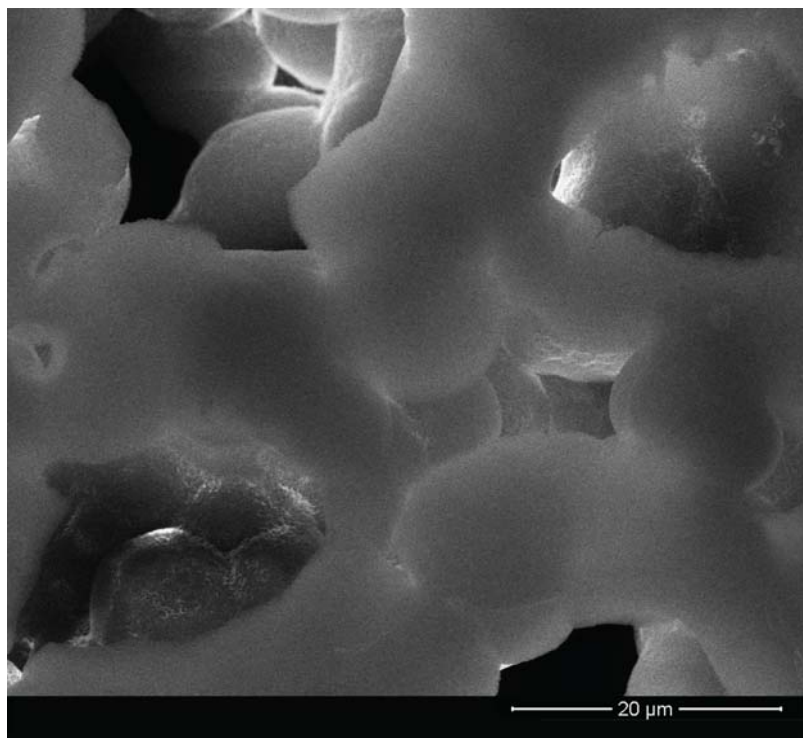
Figure 4.14 Etched Nylon 6 / E-*n*BA-MAH blend with content 90/10 w/w.
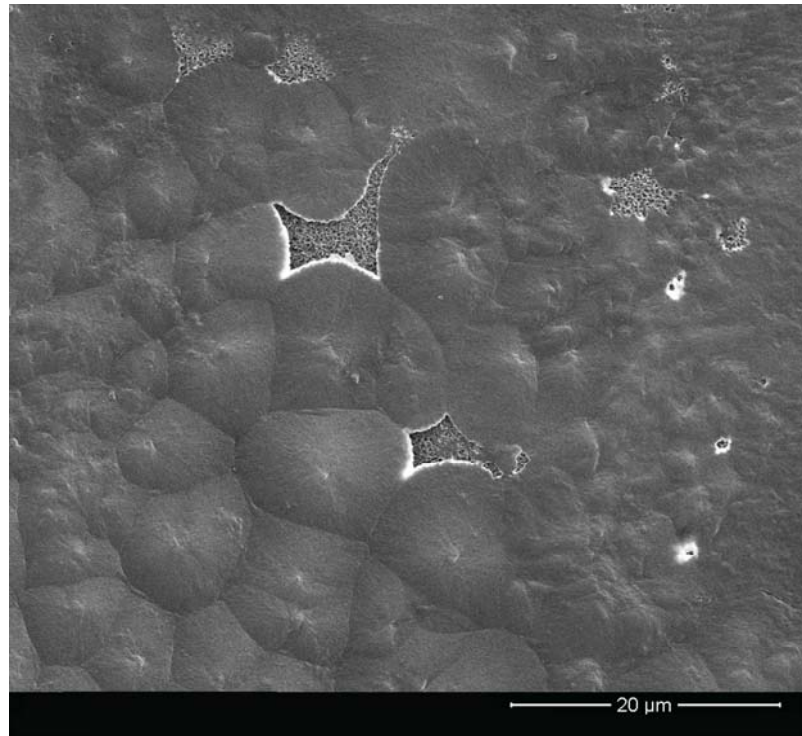
Figure 4.15 Etched Nylon 6 / E-*n*BA-MAH blend with content 85/15 w/w.

Table 4.08 Parameters of distribution function at 20 kV and 10 cm tip-to-collector distance for various E-*n*BA-MAH contents.

Parameters		E-nBA-MAH Content (w/w %)			
		0	5	10	15
N	(#)	37	68	78	70
d_{max}	(nm)	1292.70	615.79	692.04	600.49
d_{min}	(nm)	297.18	246.46	280.70	190.44
d_g	(nm)	478.83	423.27	456.25	290.97
δ		0.99	1.64	1.11	1.28

As the content of terpolymer increases, the geometric mean of the diameters of nanofibers decreases. This may be due to effect of terpolymer on the diameter. As terpolymer increases, if other conditions are set constant, terpolymer affects the mixture by increasing the flexibility and this contributes the fiber to get thinner.

Some of the diameters came out to be high, because, the diameter (0.5 mm) of the micropipette initially used was quite high. The fluid was coming down by gravity in micropipette and it was difficult to achieve stability at the tip because of the high viscosity. Another problem which showed up in the product was the formation of a web as seen from Fig. 4.16. The figure depicts nanofibers obtained from mixture D. This could be associated with the difficulty of the evaporation of solvents within a short time interval.
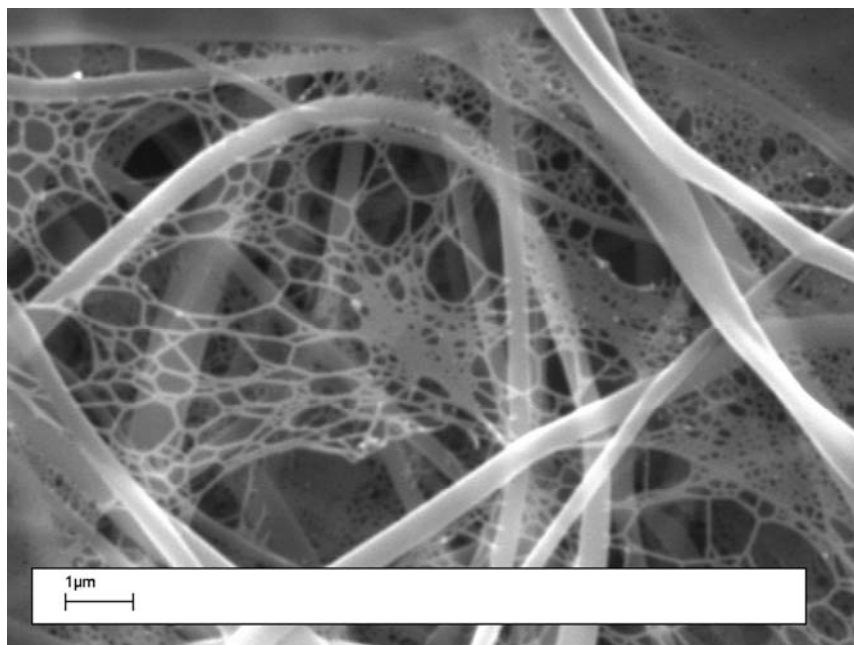
Figure 4.16 Web-like structure between electrospun fibers.

The parameter δ represents the magnitude of scatter [84]. It increases as the content of terpolymer increases, hence the terpolymer content lowers δ.

Interestingly, final estimated standardized diameter, given in Fig. 4.17, is in accordance with the interacting energy between two polymer systems given in Fig. 4.12. Interaction gets stronger somewhere after 5% elastomeric content. However, after a certain amount of elastomer content, the interaction drops down as obseved in Fig. 4.12.
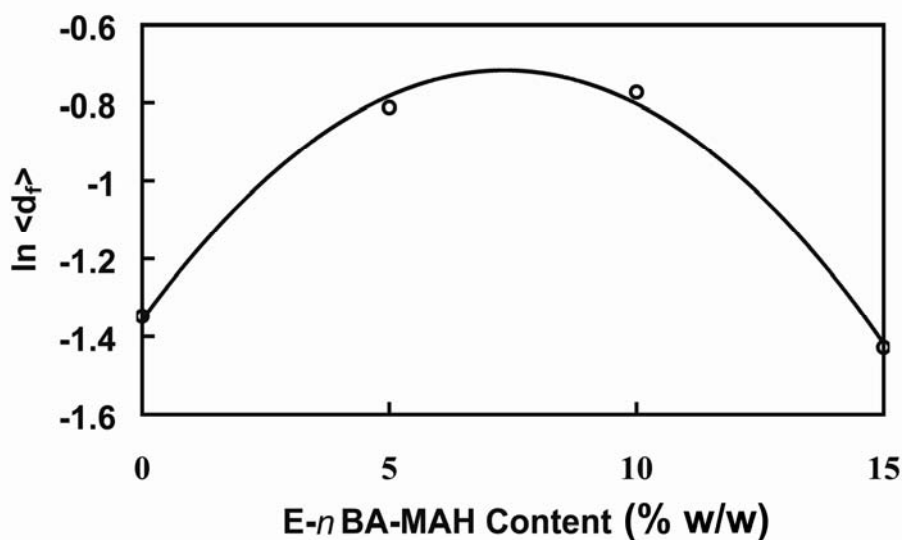
Figure 4.17 Change of $\ln\langle d_f \rangle$ with elastomer content in the blend.

4.6 The Effect of Electrical Field on the Diameter of Nanofibers

Electrical field depends on the voltage and tip-to-collector distance as indicated in Eq. 3.17. Table 4.09 lists the parameters of distribution function. The electrospinning process has various process parameters; the voltage and the tip-to-collector distance are just two of them. In the experiments, the distances considered were 10 cm, 15, and 22 cm, and the voltages applied were 15 kV, 20 kV, and 22 kV.
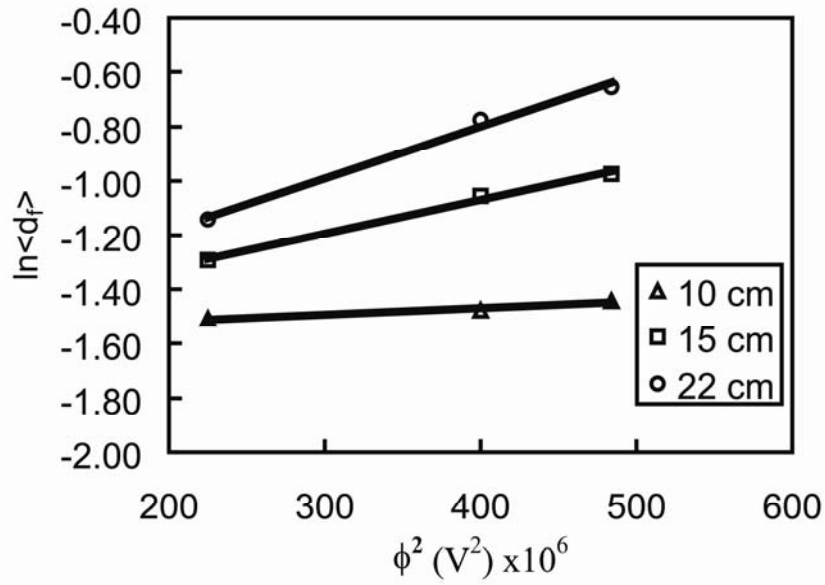
Figure 4.18 Change of $\ln\langle d_f \rangle$ with the square of electrical potential.

Table 4.09 Parameters of distribution function of nanofiber diameters at 15, 20 and 22 kV voltage and 10, 15, and 22 cm distance.

		Distance (cm)								
		10			15			22		
		Voltage (kV)			Voltage (kV)			Voltage (kV)		
Parameters		15	20	22	15	20	22	15	20	22
N	(#)	37	141	124	106	109	92	85	132	83
d_{max}	(nm)	147.6	109.7	118.6	140.4	132.0	97.8	168.3	118.7	118.3
d_{min}	(nm)	26.3	32.6	42.5	36.5	39.3	32.6	30.1	32.6	35.1
d_g	(nm)	74.2	69.3	72.0	70.3	72.3	62.5	74.0	69.2	75.23
δ			2.06	2.09	1.15	1.45	0.88	1.03	1.34	1.13	1.34

The concentration used for Nylon 6 / formic acid solution to investigate the effect of electrical field was 15% (w/v). The mean diameter of the nanofibers obtained with increasing voltage is getting thinner. However, increasing distance does not affect the diameters of nanofibers.

The broadness of distribution, namely the parameter δ has no linear correlation with the increasing voltage and/or distance. At 15 kV electrical potential increasing distance narrows the spectrum as the parameter δ increases.
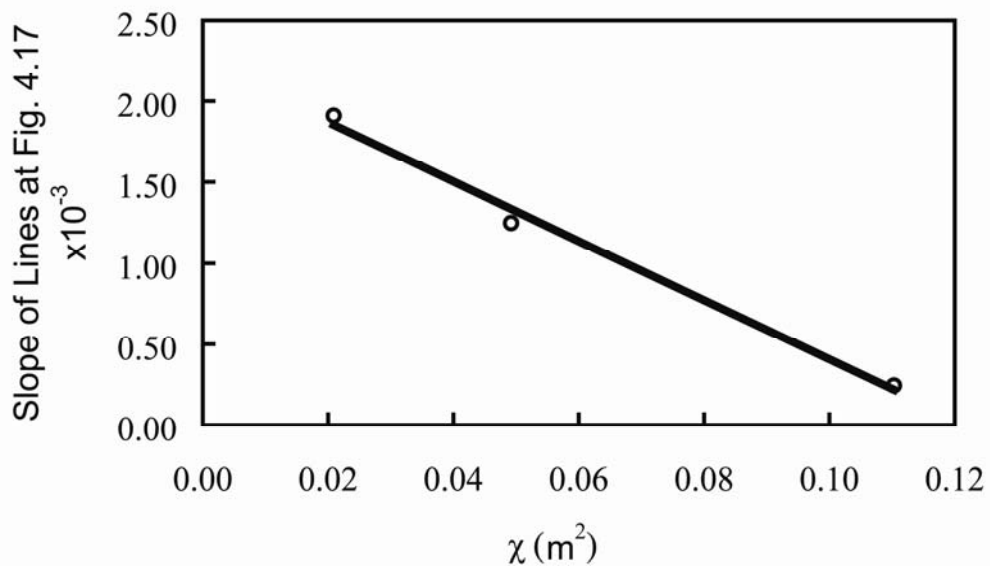
Figure 4.19 Linear relationship of the slopes of the lines in Fig.4.17, as a function of χ, with initial diameter $d_i = 0.8mm$.

The expected value of final diameter changes linearly with the square of electrical potential as seen in Fig. 4.18. There is a linear relationship between the slopes of straight lines seen in Fig.4.18 and Eq. 3.24 as seen from Fig. 4. 19. The mutual relationship of those parameters implies that electrical field has dominant role on the deformation of the polymeric jet.

4.7 Effect of Concentration on Nanofibers

The effect of concentration was studied by using 13%, 15%, and 17% Nylon 6/formic acid solution electrospun at 20 kV and at a tip-to-collector distance of 10 cm. The SEM micrographs of the nanofibers obtained from these concentrations are given in Fig. 4.20, Fig. 4.21, and Fig. 4.22, respectively. The parameters of Johnson S_B distribution function are given in Table 4.10.
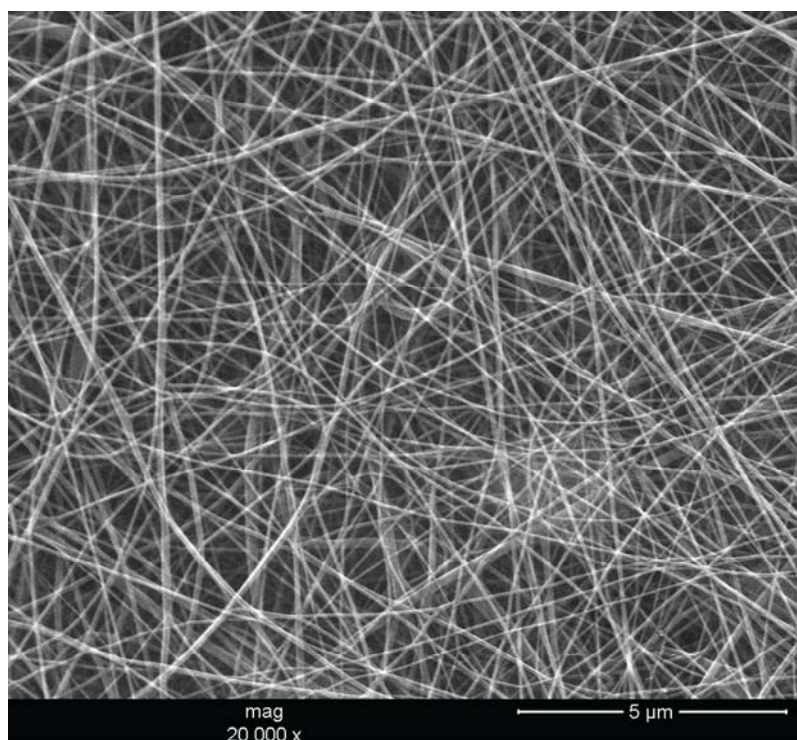
Figure 4.20 SEM image of the nanofibers obtained from
Nylon 6 (13%)-formic acid solution -.
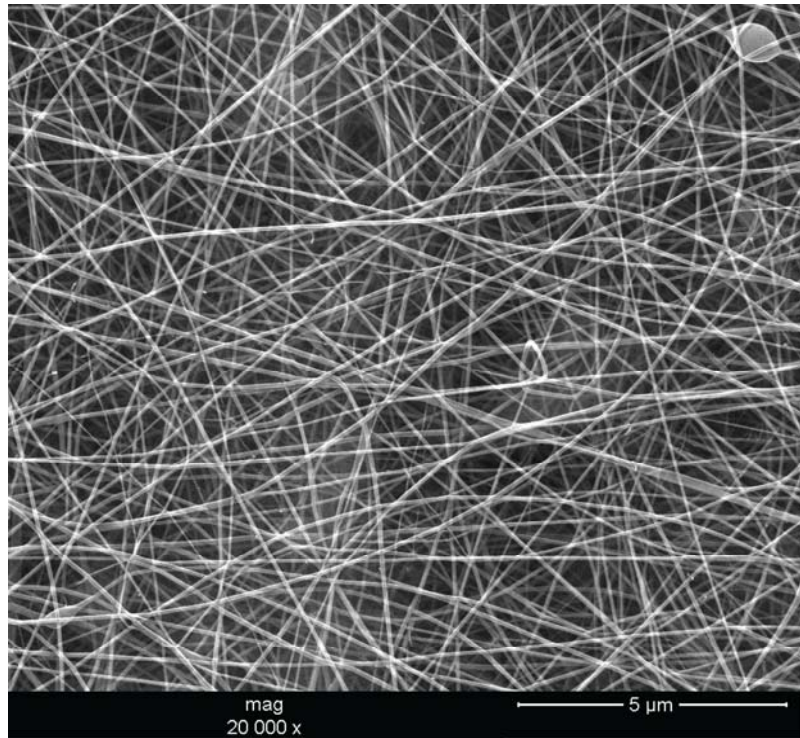
Figure 4.21 SEM image of the nanofibers obtained from
Nylon 6 (15%)-formic acid solution-.

As the solution becomes dilute condition- physical entanglement of the polymeric chains loosens and the polymer flows easily in spinning process. This results in thinner nanofibers from dilute solutions.

Fig. 4.23 shows the linear relationship between the natural logarithm of expected value of final diameter of deformed nanofiber obtained from Eq. 3.22 and the concentration of polymeric solution in electrospinning process.

Table 4.10 The parameters of the distribution function related to the Nylon 6 nanofibers (20 kV voltage and 10 cm tip-to-collector distance) from various concentrations.

Parameters	Concentration of Solution (w/v %)		
	13	15	17
N (#)	167	114	123
d_{max} (nm)	149.55	134.40	165.69
d_{min} (nm)	30.92	30.05	24.37
d_g (nm)	67.89	71.62	85.86
δ	1.20	1.14	1.12
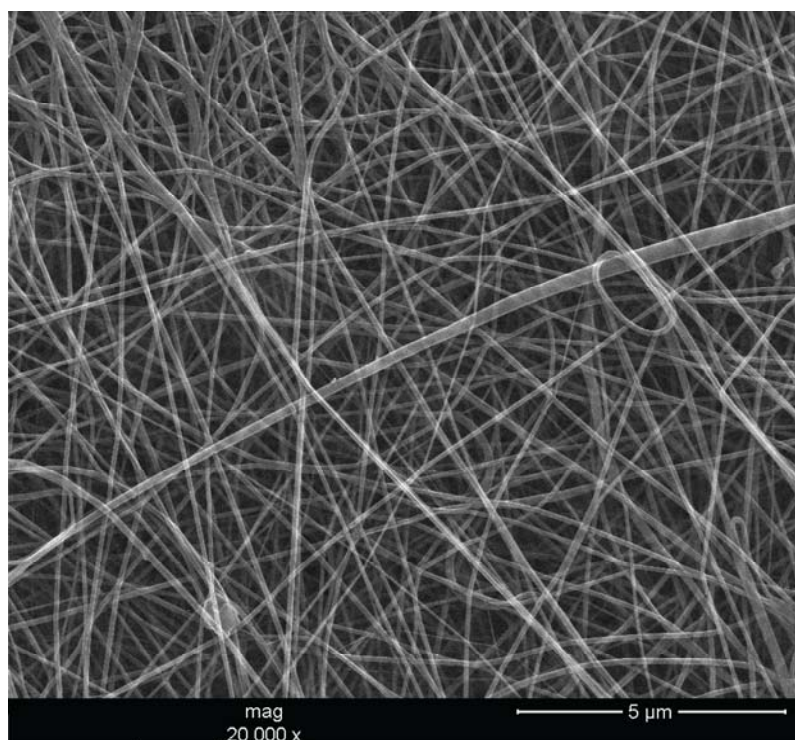
Figure 4.22 SEM image of the nanofibers obtained from Nylon 6 (17%)-formic acid solution.
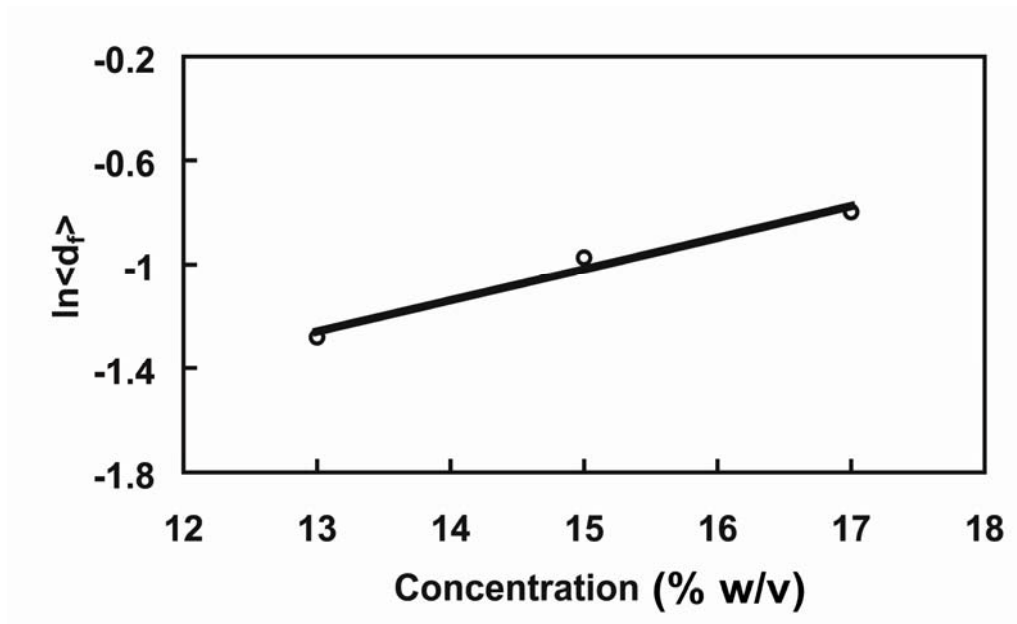
Figure 4.23 The natural logarithm of estimated final
diameter of the nanofibers obtained from
Eq. 3.21, Change of $\ln\langle d_f \rangle$, with the
concentration (C) of Nylon 6/formic acid
solution.

4.8 Effect of Needle Size on Nanofibers

Nylon 6/ formic acid solution with 15% (w/v) concentration was electrospun under the conditions of 20 kV electrical potential and 10 cm distance tip-to--collector distance. The needle of the syringe mounted at the pump - was set to 5 µl/min rate. Needles of three different diameters were used in the experiments; these are 0.8 mm, 0.90 mm, and 1.20 mm. Table 4.11 gives the parameters of the distribution function related to the diameters of the nanofibers The mean diameter of the fibers slightly increases with the increase of the needle diameter, meanwhile δ also increases indicating that more uniformly sized nanofibers are obtained.

The relation between the logarithm of the expected value of the diameters of nanofibers obtained from Eq. 3.22 and the needle diameter is shown in Fig. 4.24. It is seen that there is significant effect of needle diameter.

Table 4.11 The parameters of the distribution function related to the Nylon 6 nanofibers (20 kV and 10 cm tip-to-collector distance) from various needles.

Parameters	Diameter of Needle (mm)		
	0.80	0.90	1.20
N (#)	108	123	127
d_{max} (nm)	347.744	305.22	315.89
d_{min} (nm)	42.17	32.89	36.77
d_g (nm)	95.86	105.56	104.14
δ	.37	1.68	1.75
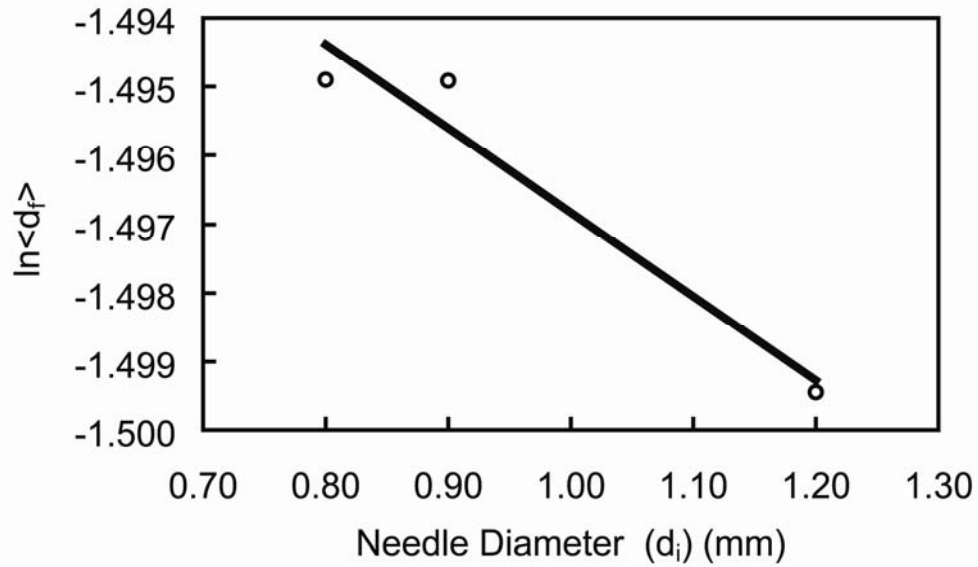
Figure 4.24 The change of expected $\ln\langle d_f \rangle$ with needle diameter (d_i).

4.9 Effect of Feed Rate on Nanofibers

The effect of the feed rate on the distribution of diameters of nanofibers can be investigated by keeping the other parameters constant. The feed rate of the syringe was set to 3 µl/min, 5 µl/min, and 10 µl/min while the solution of Nylon 6/formic acid with 15% (w/v) concentration in the syringe was electrospun at 20 kV electrical potential and 10 cm tip-to-collector distance. Table 4.12 lists the statistical parameters of resultant nanofibers. The $\ln\langle d_f \rangle$ changes linearly with the flow rate as seen from Fig. 4.25. The mean diameter decreases with increasing flow rate of the solution. The parameter δ decreases with high feed rates. It indicates that the distribution gets broader and homogeneity of nanofibers is lost.

Table 4.12 The parameters of the distribution function related to the Nylon 6
nanofibers (20 kV and 10 cm tip-to-collector distance) at various
feed rates.

Parameters	Feed Rate (µl/min)		
	3	5	10
N (#)	104	106	106
d_{max} (nm)	206.82	140.40	135.18
d_{min} (nm)	29.30	36.50	36.34
d_g (nm)	80.23	70.33	67.32
δ	1.63	1.46	1.17
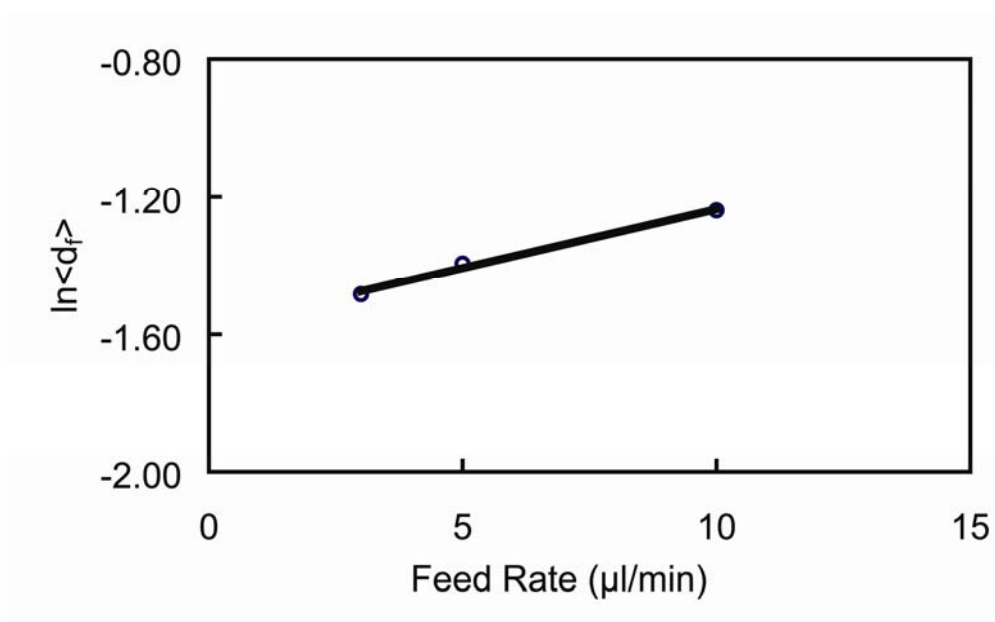
Figure 4.25 The change of $\ln\langle d_f \rangle$ with feed rate (Q).

4.10 Statistical Analysis

Eq. 3.23 gives the relation between the deformation power and feed rate of solution jet, permittivity of solution system, electrical potential of process, distance to collector, the expected value, and initial diameter of solution jet. The increase of the expected value of nanofibers results in increase of the deformation power. Table 4.13 gives the fitted equations of the curves given in Fig 4.17, 4.19, 4.23, 4.24 and 4.25. Correlation coefficients close to unity indicates a relatively good agreement between experimental observations and estimations of equations. It is concluded that the applied electrical field and the concentration are primary parameters, and the needle diameter of the syringe and the feed rate of the solution have relatively minor effect.

Table 4.13 Fitted equations and R^2 values of the curves given in Fig. 4.17, 4.19, 4.23, 4.24, and 4.25.

Parameters	Fitted Equation	R^2
E-nBA-MAH Content (%Ce) (w/w)	$\ln\langle d_f \rangle = -0.01C_e{}^2 + 0.18C_e - 1.36$	0.995
Electrical Field (E) (V/m)	$\ln\langle d_f \rangle \propto 19.4E^2$	
Concentration (%C) (w/v)	$\ln\langle d_f \rangle = 0.12C - 2.82$	0.975
Needle Diameter (d_i)(mm)	$\ln\langle d_f \rangle = -0.01d_i - 1.49$	0.943
Feed Rate (Q) (µl/min)	$\ln\langle d_f \rangle = 0.03Q - 1.58$	0.992

4.11 The Effect of Collector Design on Nanofibers

In electrospinning, the electrified solution jet tries to follow the electrical field field lines. The resultant nanofibers are affected by the design

of the collector. The designs of different collectors are studied to investigate the design influence on the morphology of resultant nanofibers.

4.11.1 Flat Surface Area of Collector

Table 4.13 gives the parameters of distribution function of the nanofibers obtained from 15% (w/v) Nylon6/ formic acid solution, electrospun under 20 kV and 10 cm distance, and collected at two collectors which have 80 mm x 80 mm and 200 mm x 400 mm dimensions. The mean diameter increases as the surface area of the collector increases. The value of δ also increases with increasing surface area of collector. It implies that large collector improves homogeneity.

Table 4.14 Parameters of distribution function of Nylon6 nanofibers (20 kV, 10 cm tip-to-collector distance).

Parameters	Area of Flat Surface (mm x mm)	
	80 x 80	200 x 400
N (#)	68	60
d_{max} (nm)	188.67	310.38
d_{min} (nm)	49.33	55.48
d_g (nm)	99.81	109.58
δ	1.13	1.46

4.11.2 Parallel Plates

Using parallel collector plates is possible as seen from Fig. 4.27. Nanofibers follow the electrical field lines and deposit between the parallel

plates orienting at the direction of normal vector of parallel plates. The distance between the parallel plates are 160 mm The nanofibers collected at the gap between the plates are shown in Fig. 4.27. The distribution of the angles between normal vector and the direction of nanofibers is depicted in Fig. 4.28. Half of the nanofibers is in the direction of normal vector but the distribution has bimodal characteristics at the vicinity of 30° and 0° which is the direction of normal vector.
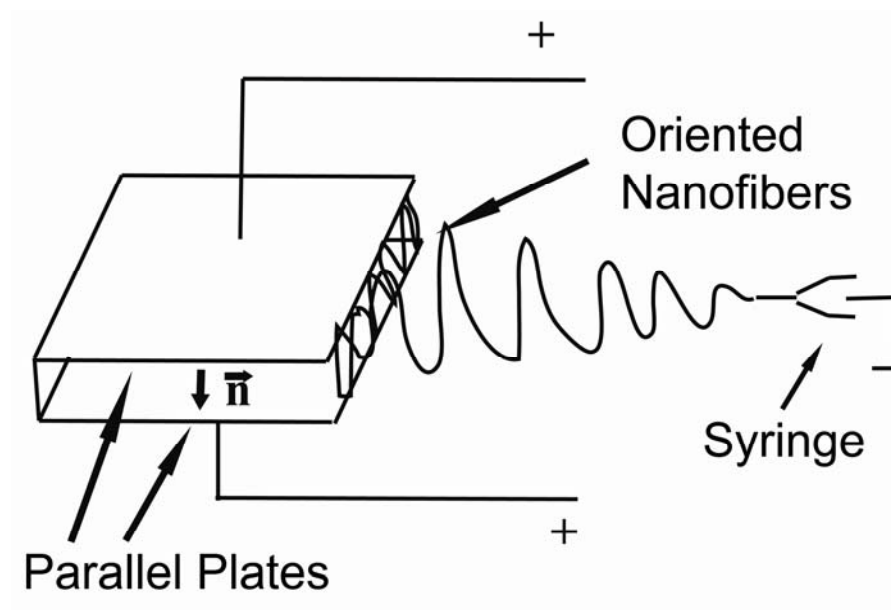
Figure 4.26 Normal vector and electrospinning setup.
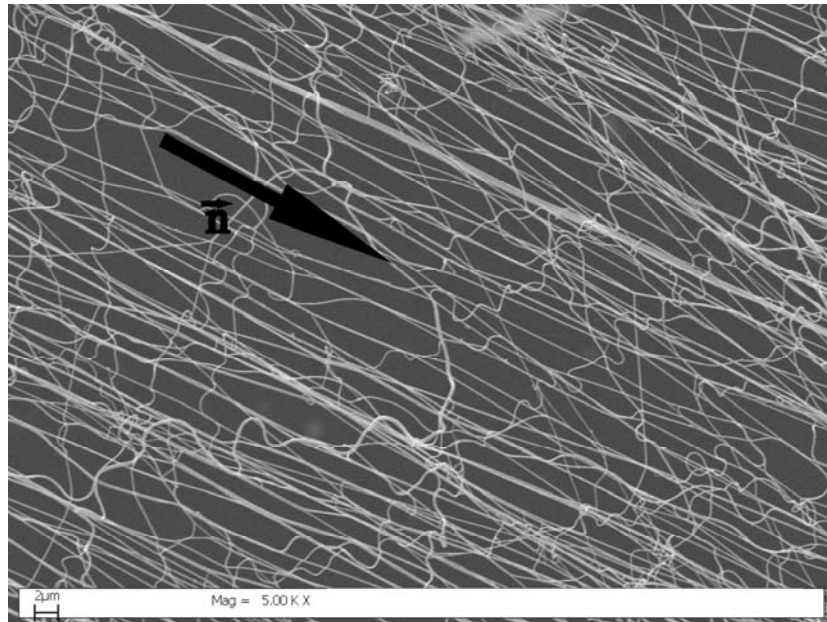
Figure 4.27 Normal vector and oriented nanofibers collected on parallel plates.
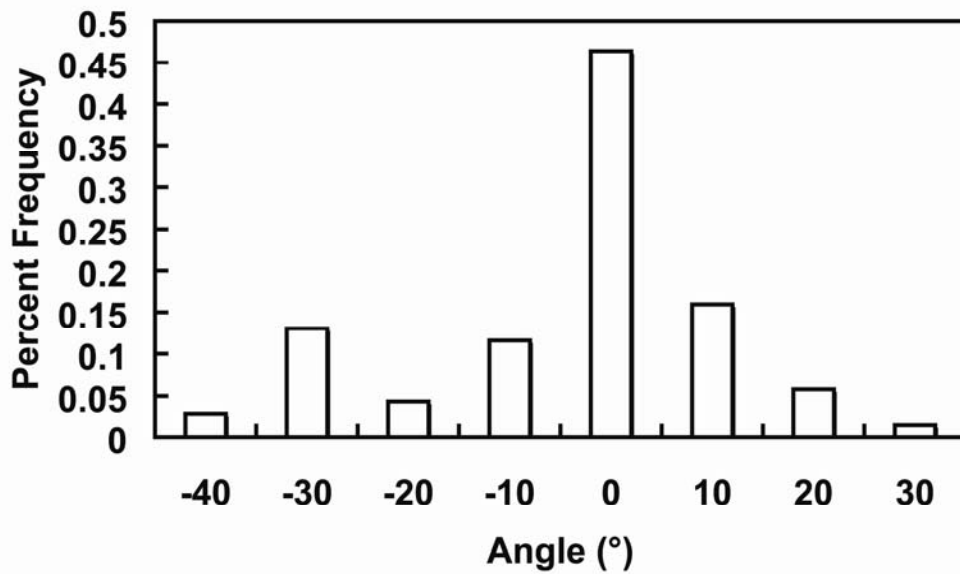
Figure 4.28 The distribution chart of the angles between normal vector shown in Fig. 4.26 and the directions of nanofibers.

4.11.3 Capillary Distance

The distance between parallel plates were set to a gap of 200 µm. A few nanofibers were collected on the gap as seen in Fig. 4.29. The individual single nanofiber was collected at such gap (Fig 4.30). Characterization of a single nanofiber can be possible by producing single nanofiber by this technique.
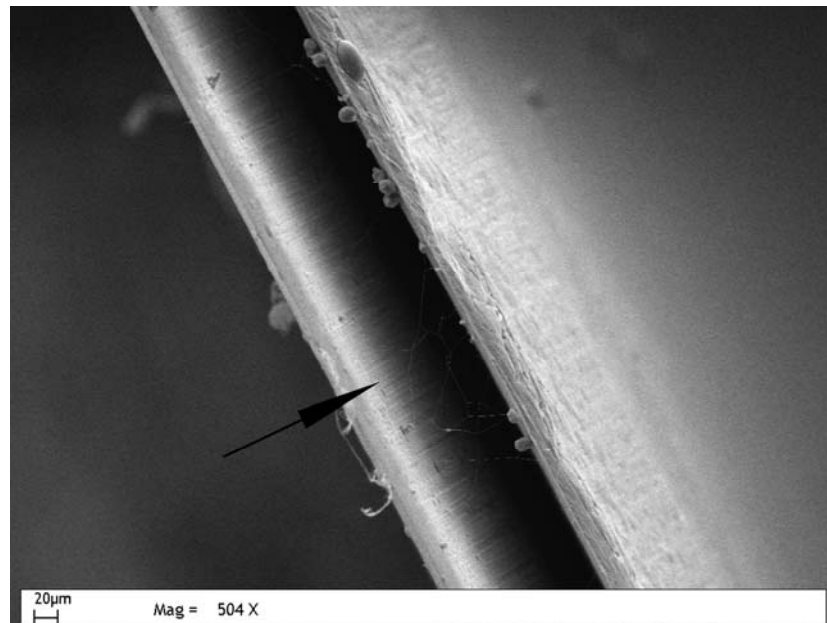
Figure 4.29 Nanofibers obtained at capillary distance.
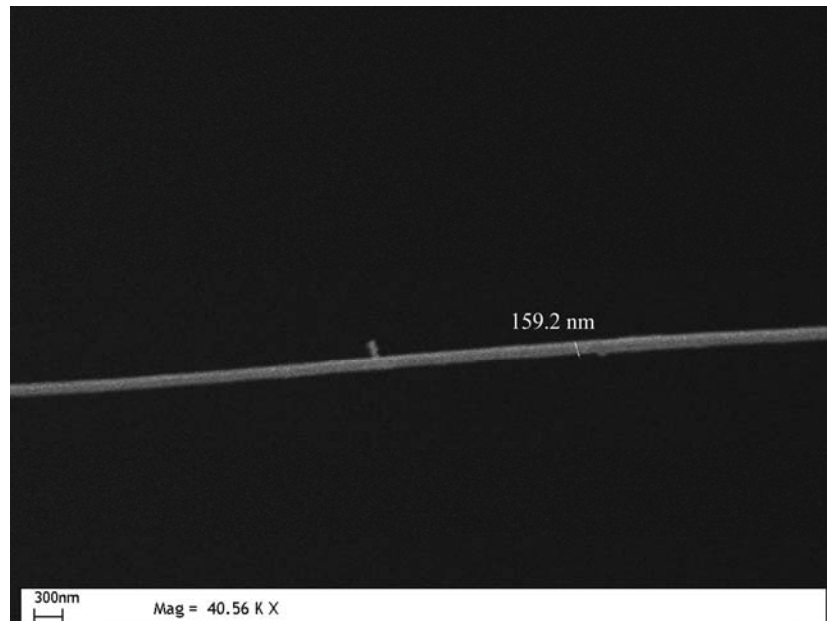
Figure 4.30 Single nanofiber.

4.12 Mechanical Analysis of Nanofibers

The calculated elastic modulus to viscous modulus ratio ψ which is given in Eq. 3.32 for several points along single nanofibers obtained from neat Nylon 6 is seen in Fig. 4.31. The figure is obtained from the slopes described in Fig. 3.10.
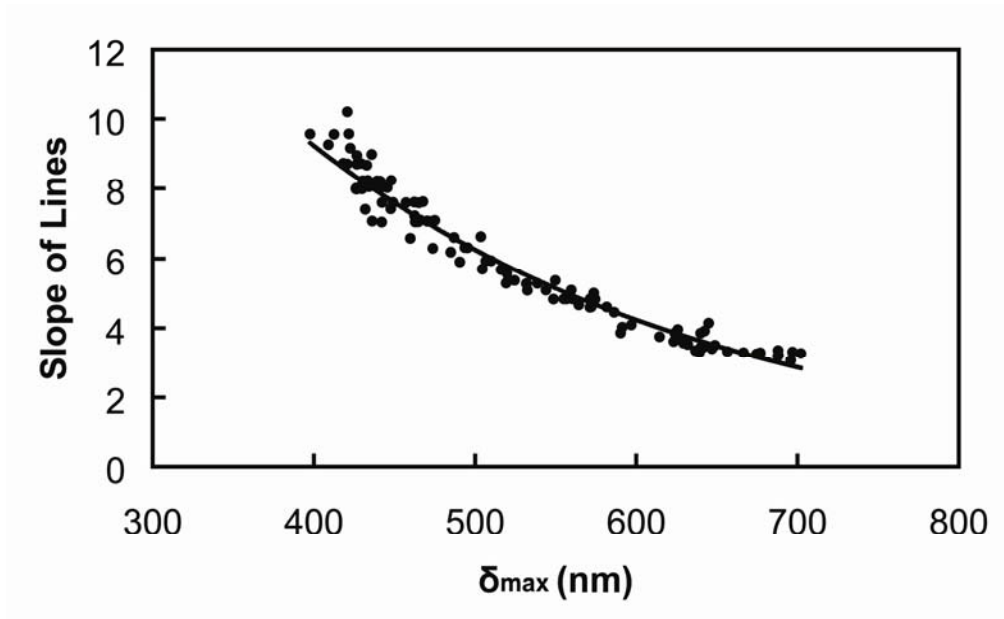
Figure 4.31 Calculated ratio ψ for several points along single nanofibers obtained from neat Nylon 6

It is obvious that the ratio of elastic modulus to viscous modulus (ψ) is a function of maximum indentation (δ_{max}). The fitted curve function is given as,

$$\psi = \psi_o \exp(-\delta_o \delta_{max})$$

(4.01)

where, ψ_o is preexponential term, and δ_o is maximum indentation coefficient. Due to the constant value of force and distance limits, maximum indentation value is correlated with nanofiber diameter. Hence, ψ_o can be read as the inverse of relaxation time and δ_o can be read as sensitivity to diameter. Fig. 4.32 gives the constants of ψ_o and δ_o with various impact modifier contents. The correlation coefficients (R^2) for the neat Nylon 6 (0 w/w %), and blends that contain 5 % (w/w), 10 % (w/w), and 15 % (w/w) terpolymer are 0.97,

0.94, 0.98, and 0.83, respectively. The observation numbers (N) for the same compositions are 120, 78, 107, and 94, respectively.
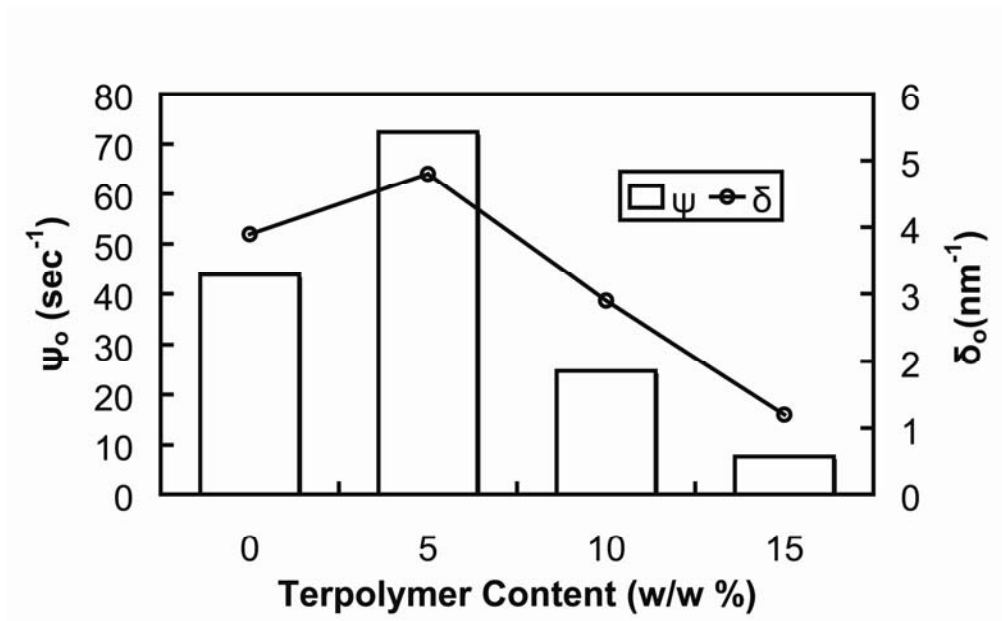
Figure 4.32 The constants of ψ_o and δ_o with various impact modifier contents

CHAPTER 5

CONCLUSIONS

Excluding the crystalline structure effect, the bare interaction energy between Nylon 6 and *E-nBA-MAH* terpolymer is calculated according to melting point depression approach using both the Flory Huggins (FH) theory and the Sanchez-Lacombe Equation of State (SL EOS). The bare interaction energy given by two theories has negative value. It implies that at all compositions and temperatures the two systems do not show phase separation by excluding the crystalline structures. However, at room temperature WAXS analysis gives the information that varying composition of blends also has altering crystalline structures.

The crystalline morphology and crystal thickness hinders the compatibility of the two polymers. Isothermal kinetics analysis reveals that the most favorable interaction between them is seen at 5% *E-nBA-MAH content* by reducing the crystallinity of Nylon 6. Also, 5% addition of *E-nBA-MAH* into Nylon 6, allocates it to form stable α-crystalline phase due to the polarity of the butyl acrylate group of *E-nBA-MAH* terpolymer.

After a certain amount of *E-nBA-MAH* addition (between %10 and 15% of blend weight) into Nylon 6, the polymers in the system form their individual crystalline structures. The SEM micrographs support that they show phase separation due to strong crystalline structure of Nylon 6. Although the blends are thermodynamically favorable, strong secondary structure of Nylon 6 does not allow penetration into the sites as seen in

WAXS analysis, crystallization kinetics and SEM micrographs, and the crystallinity goes up almost to the level of plain Nylon 6.

Investigation of electrospinning is very challenging because of the interaction of parameters on the resultant nanofibers. However, *ceteris paribus* approach makes the investigation more applicable.

The research showed that deforming power has relevance with the interaction capability of two polymers as seen in statistical analysis and crystallization kinetics. Having mixed with 5% of the total mixture by weight assists the second component, E-nBA-MA, to interact with main phase, Nylon 6, more readily. This finding is supported by both the compatibility analysis and statistical analysis of the polymers.

The design of the collector also affects the resultant nanofibers. Moreover, changing of the flat surface area has influence on the nanofibers collected on it The large surface area gives more homogenous nanofibers. Collection at the gap of two parallel plates results in oriented nanofibers.

The mechanical characterization procedure proposed in the study gives reasonable results and in accord with the crystallization kinetics and statistical characterization work. The nanofiber that contains 5% (w/w) shows lower relaxation time. Adding more impact modifier increases the relaxation time and due to loosening of the strength of the interaction. The best composition is 5% elastomer content which has the strongest interaction.

Sensitivity to diameter increases after to 5%(w/w) content. This result reveals that elastomer makes nanofibers more non-sensitive to the thickness of nanofibers.

.

APPENDIX A

FIRST AND SECOND MOMENTS OF ESTIMATED DIAMETER

The first moment of estimated diameter [85] $\langle d \rangle = \dfrac{\phi}{\psi}$

where $\phi = A - B$ and $\psi = CD$,

and,

$$A = \frac{1}{2\delta} + \frac{1}{2\delta} \sum_{n=1}^{\infty} \exp(-n^2/2\delta^2) \cosh\left(\frac{n(1-2\delta\gamma)}{2\delta^2}\right) \sec h\left(\frac{n}{2\delta^2}\right)$$

$$B = 2\pi\delta \sum_{n=1}^{\infty} \exp\left(-\frac{1}{2}(2n-1)^2 \pi^2\delta^2\right) \sin((2n-1)\pi\delta\gamma)\cos ech((2n-1)\pi^2\delta^2)$$

$$C = 1 + 2\sum_{n=1}^{\infty} \exp(-2n^2\pi^2\delta^2)\cos(2n\pi\delta\gamma)$$

$$D = \sqrt{2\pi}\, 2\exp\left(\frac{\delta^2}{2}\right)$$

where, γ is the parameter of Jonson S_B distribution function. When the minimum and maximum values are known a priori, maximum likelihood estimates the parameter γ,

$$\hat{\gamma} = -\frac{\bar{f}}{S_f}$$

where $f = \ln\left(\dfrac{y}{1-y}\right)$ and $\bar{f}$ is the sample mean.

The second moment of the estimated diameter $\langle d^2 \rangle$ is given by,

$$\langle d^2 \rangle = \langle d \rangle (1 - \delta\gamma) + \frac{\delta}{\psi}\left[\frac{\partial A}{\partial \gamma} - \frac{\partial B}{\partial \gamma} - \langle d \rangle \frac{\partial C}{\partial \gamma} D\right]$$

The partial derivations are given as,

$$\frac{\partial A}{\partial \gamma} = -\frac{1}{2\delta^2}\sum_{n=1}^{\infty} n \exp(-n^2/2\delta^2)\sinh\left(\frac{n(1-2\delta\gamma)}{2\delta^2}\right)\sec h\left(\frac{n}{2\delta^2}\right)$$

$$\frac{\partial B}{\partial \gamma} = 2(\pi\delta)^2\sum_{n=1}^{\infty} (2n-1)\exp\left(-\frac{1}{2}(2n-1)^2\pi^2\delta^2\right)\cos((2n-1)\pi\delta\gamma)\cos ech\left((2n-1)\pi^2\delta^2\right)$$

$$\frac{\partial C}{\partial \gamma} = -4\pi\delta\sum_{n=1}^{\infty} n \exp\left(-2n^2\pi^2\delta^2\right)\sin(2n\pi\delta\gamma)$$

REFERENCES

1. Ramakrishna, S., *An introduction to electrospinning and nanofibers*. 2005, New Jersey [u.a.]: World Scientific.

2. Gonzalez, I., J.I. Eguiazabal, and J. Nazabal, *Rubber-toughened polyamide 6/clay nanocomposites.* Composites Science and Technology, 2006. **66**(11-12): p. 1833-1843.

3. Kumar, S., B.V. Ramanaiah, and A.R. Ray, *Studies on impact toughening and thermal properties of nylon-6/ LDPE-g-MAH blends.* Polymer - Plastics Technology and Engineering, 2006. **45**(9): p. 1039-1046.

4. Yasaku, W. and K. Tetsuo, *Relation between impact strength and dynamic mechanical properties of plastics.* Journal of Applied Polymer Science, 1967. **11**(9): p. 1661-1665.

5. Huang, Z.M., et al., *A review on polymer nanofibers by electrospinning and their applications in nanocomposites.* Composites Science and Technology, 2003. **63**(15): p. 2223-2253.

6. Rutledge, G.C. and S.V. Fridrikh, *Formation of fibers by electrospinning.* Advanced Drug Delivery Reviews, 2007. **59**(14): p. 1384-1391.

7. Koski, A., K. Yim, and S. Shivkumar, *Effect of molecular weight on fibrous PVA produced by electrospinning.* Materials Letters, 2004. **58**(3-4): p. 493-497.

8. Wongsasulak, S., et al., *The effect of solution properties on the morphology of ultrafine electrospun egg albumen-PEO composite fibers.* Polymer, 2007. **48**(2): p. 448-457.

9. Cui, W., et al., *Investigation on process parameters of electrospinning system through orthogonal experimental design.* Journal of Applied Polymer Science, 2007. **103**(5): p. 3105-3112.

10. Bhattacharjee, P.K., et al., *On the measured current in electrospinning.* Journal of Applied Physics. **107**(4): p. 044306-7.

11. Reneker, D.H. and A.L. Yarin, *Electrospinning jets and polymer nanofibers.* Polymer, 2008. **49**(10): p. 2387-2425.

12. Macossay, J., et al., *Effect of needle diameter on nanofiber diameter and thermal properties of electrospun poly(methyl methacrylate).* Polymers for Advanced Technologies, 2007. **18**(3): p. 180-183.

13. Li, D., Y. Wang, and Y. Xia, *Electrospinning of Polymeric and Ceramic Nanofibers as Uniaxially Aligned Arrays.* Nano Letters, 2003. **3**(8): p. 1167-1171.

14. Ishii, Y., H. Sakai, and H. Murata, *A new electrospinning method to control the number and a diameter of uniaxially aligned polymer fibers.* Materials Letters, 2008. **62**(19): p. 3370-3372.

15. Theron, A., E. Zussman, and A.L. Yarin, *Electrostatic field-assisted alignment of electrospun nanofibres.* Nanotechnology, 2001(3): p. 384.

16. Lee, K.-H., et al., *Polarized FT-IR Study of Macroscopically Oriented Electrospun Nylon-6 Nanofibers.* Macromolecules, 2008. **41**(4): p. 1494-1498.

17. Jun, K. and H.G. Craighead, *Fabrication of oriented polymeric nanofibers on planar surfaces by electrospinning.* Applied Physics Letters, 2003. **83**(2): p. 371-373.

18. Kenawy, E., et al., *Processing of Polymer Nanofibers Through Electrospinning as Drug Delivery Systems*, in *Nanomaterials: Risks and Benefits*. 2009. p. 247-263.

19. Pham, Q.P., U. Sharma, and A.G. Mikos, *Electrospinning of Polymeric Nanofibers for Tissue Engineering Applications: A Review.* Tissue Engineering, 2006. **12**(5): p. 1197-1211.

20. Lannutti, J., et al., *Electrospinning for tissue engineering scaffolds.* Materials Science and Engineering: C, 2007. **27**(3): p. 504-509.

21. Shin, Y.M., et al., *Experimental characterization of electrospinning: the electrically forced jet and instabilities.* Polymer, 2001. **42**(25): p. 09955-09967.

22. Li, D. and Y. Xia, *Direct Fabrication of Composite and Ceramic Hollow Nanofibers by Electrospinning.* Nano Letters, 2004. **4**(5): p. 933-938.

23. Jeong, J.S., et al., *Fabrication of MWNTs/nylon conductive composite nanofibers by electrospinning.* Diamond and Related Materials. **15**(11-12): p. 1839-1843.

24. Jose, M.V., et al., *Morphology and mechanical properties of Nylon 6/MWNT nanofibers.* Polymer, 2007. **48**(4): p. 1096-1104.

25. Chronakis, I.S., *Novel nanocomposites and nanoceramics based on polymer nanofibers using electrospinning process--A review.* Journal of Materials Processing Technology, 2005. **167**(2-3): p. 283-293.

26. Ramani, M.V., et al., *Vapor-Liquid Equilibrium for Polymer-Diluent Systems from Melting Point Depression.* Industrial and Engineering Chemistry Research, 2004. **43**(4): p. 1144-1149.

27. Rostami, S.D., *Advances in theory of equilibrium melting point depression in miscible polymer blends.* European Polymer Journal, 2000. **36**(10): p. 2285-2290.

28. Linares, A. and J.L. Acosta, *Compatibility studies of partially compatible blends through glass transition temperature and melting point depression analysis.* Journal of Applied Polymer Science, 1998. **67**(6): p. 997-1004.

29. Gan, L.H. and K.K. Chee, *Binary interactions in dimethyl terephthalate/bis(2-ethylhexyl)adipate/poly(vinyl chloride) blends studied by melting point depression method.* Journal of Applied Polymer Science, 1996. **60**(2): p. 271-278.

30. Tang, M.-Y. and S.L. Kim, *Poly(ethylene terephthalate)-solvent interaction: gelation and melting point depression.* Polymer Engineering and Science, 1994. **34**(22): p. 1656-1663.

31. McGuire, K.S., A. Laxminarayan, and D.R. Lloyd, *Simple method of extrapolating the coexistence curve and predicting the melting point depression curve from cloud point data for polymer-diluent systems.* Polymer, 1994. **35**(20): p. 4404-4407.

32. Pengtao Huo, P. and P. Cebe. *Melting point depression in poly(butylene terephthalate)/polyarylate blends.* 1993. Denver, CO, USA: Publ by ACS, Washington, DC, USA.

33. Runt, J. and K.P. Gallagher, *Polymer-polymer interaction parameters via melting point depression. A critical analysis.* Polymer Communications (Guildford, England), 1991. **32**(6): p. 180-182.

34. Jo, W.H. and I.H. Kwon, *Equation of state theory for melting point depression in miscible polymer blends.* Macromolecules, 1991. **24**(11): p. 3368-3372.

35. Shenoy, S.L., P.C. Painter, and M.M. Coleman. *Melting point depression in crystalline/amorphous polymer blends that hydrogen bond*. 1990. Boston, MA, USA: Publ by ACS, Washington, DC, USA.

36. Bohdanecky, M., L. Simek, and S. Petrik, *Estimation of the polymer-polymer interaction parameter from the melting point depression of crystalline oligomers.* Polymer Communications (Guildford, England), 1990. **31**(4): p. 137-139.

37. Nishio, Y., et al., *Cellulose/poly(vinyl alcohol) blends: An estimation of thermodynamic polymer-polymer interaction by melting point depression analysis.* Macromolecules, 1989. **22**(5): p. 2547-2549.

38. Sanchez, I.C. and R.H. Lacombe, *An elementary molecular theory of classical fluids. Pure fluids.* J. Phys. Chem., 1976. **80**(21): p. 2352-2362.

39. Isaac C. Sanchez, R.H.L., *An elementary equation of state for polymer liquids.* Journal of Polymer Science: Polymer Letters Edition, 1977. **15**(2): p. 71-75.

40. Sanchez, I.C. and R.H. Lacombe, *Statistical Thermodynamics of Polymer Solutions.* Macromolecules, 1978. **11**(6): p. 1145-1156.

41. C. K. Kim, D.R.P., *Characterization of ternary blends containing polycarbonate, tetramethyl polycarbonate, and poly (ε;-caprolactone).* Polymer Engineering & Science, 1994. **34**(1): p. 24-32.

42. Fallahi E. , B.M., Haghighat Kish M., *Micro and nano fibrils from polypropylene/nylon 6 blends.* Journal of Applied Polymer Science, 2008. **108**(3): p. 1473-1481.

43. Asadinezhad A., J.S.H., Khonakdar S. H. , Böhme F. , Hässler R., Häussler L., *Kinetics of isothermal crystallization and subsequent melting behavior of PTT/PA12 blend.* Journal of Applied Polymer Science, 2007. **106**(3): p. 1964-1971.

44. Li Cui, J.-T.Y.K.W.Q.F., *Miscibility and isothermal crystallization behavior of polyamide 6/poly(vinyl alcohol) blend.* Journal of Polymer Science Part B: Polymer Physics, 2008. **46**(13): p. 1360-1368.

45. Kevin Urman, J.O., *Novel phosphate glass/polyamide 6 hybrids: Miscibility, crystallization kinetics, and mechanical properties.* Journal of Polymer Science Part B: Polymer Physics, 2006. **44**(2): p. 441-450.

46. Biaobing Wang, G.H.L.W., *Melting behavior, nonisothermal crystallization kinetics, and morphology of PP/nylon 11/EPDM-g-MAH blends.* Journal of Applied Polymer Science, 2008. **107**(5): p. 3013-3022.

47. G. Prasath Balamurugan, S.N.M., *Nonisothermal crystallization kinetics of polyamide 6 and ethylene-co-butyl acrylate blends.* Journal of Applied Polymer Science, 2008. **107**(4): p. 2414-2435.

48. Huang, J.-W., et al., *Crystallization kinetics and nucleation parameters of Nylon 6 and poly(ethylene-co-glycidyl methacrylate) blend.* Thermochimica Acta, 2008. **468**(1-2): p. 66-74.

49. Richao Zhang, Y.H.M.M.Y.G.A.L.Z.L., *Nonisothermal crystallization of polyamide 66/poly(phenylene sulfide) blends.* Journal of Applied Polymer Science, 2008. **107**(4): p. 2600-2606.

50. Moly, K.A., et al., *Nonisothermal crystallisation, melting behavior and wide angle X-ray scattering investigations on linear low density polyethylene (LLDPE)/ethylene vinyl acetate (EVA) blends: Effects of compatibilisation and dynamic crosslinking.* European Polymer Journal, 2005. **41**(6): p. 1410-1419.

51. Fibers, Y., *Nylon Chain Report 2008*. 2009.

52. Zhao, L., et al., *On the use of pressure-volume-temperature data of polyethylene liquids for the determination of their solubility and interaction parameters.* Polymer Engineering and Science, 2004. **44**(5): p. 853-860.

53. James P. Parker, P.H.L., *On the crystal structure of nylon 6.* Journal of Applied Polymer Science, 1977. **21**(3): p. 821-837.

54. Bellinger, M.A., et al., *Structure and Morphology of Nylon 4 Chain-Folded Lamellar Crystals.* Macromolecules, 1994. **27**(8): p. 2130-2135.

55.	Nishi, T. and T.T. Wang, *Melting Point Depression and Kinetic Effects of Cooling on Crystallization in Poly(vinylidene fluoride)-Poly(methyl methacrylate) Mixtures.* Macromolecules, 1975. **8**(6): p. 909-915.

56.	Avarami, M.J., Chem Phys, 1939. **7**(1103).

57.	Liu, M., et al., *Melting behaviors, isothermal and non-isothermal crystallization kinetics of nylon 1212.* Polymer, 2003. **44**(8): p. 2537-2545.

58.	Turbull, D. and J.C. Fisher, J. Chem Phys, 1949. **17**: p. 71.

59.	Lin, C., Polymer Engineering & Science, 1983. **23**: p. 113.

60.	Allen, T., *Particle Size Measurement.* Particle Technology Series. Vol. 7. 1997, Hockessin, DE, USA: Springer Verlag.

61.	Doghieri, F. and G.C. Sarti, *Nonequilibrium lattice fluids: A predictive model for the solubility in glassy polymers.* Macromolecules, 1996. **29**(24): p. 7885-7896.

62.	Dosunmu, O.O., et al., *Electrospinning of polymer nanofibres from multiple jets on a porous tubular surface.* Nanotechnology, 2006. **17**(4): p. 1123-1127.

63.	Flynn, M.R., *The 4-Parameter Lognormal (SB) Model of Human Exposure.* Ann Occup Hyg, 2004. **48**(7): p. 617-622.

64.	Tan, E.P.S. and C.T. Lim, *Mechanical characterization of nanofibers-a review.* Composites Science and Technology, 2006. **66**(9): p. 1102-1111.

65.	Mark, R.V., et al., *Nanoindentation of polymers: an overview.* Macromolecular Symposia, 2001. **167**(1): p. 15-44.

66.	Hwang, K.Y., et al., *Mechanical characterization of nanofibers using a nanomanipulator and atomic force microscope cantilever in a scanning electron microscope.* Polymer Testing, 2010. **29**(3): p. 375-380.

67.	Moeller, G. and V. Domnich, *AFM Nanoindentation of Polymers.* Microscopy and Microanalysis, 2007. **13**(SupplementS02): p. 186-187.

68.   Tranchida, D., S. Piccarolo, and M. Soliman, *Nanoscale Mechanical Characterization of Polymers by AFM Nanoindentations: Critical Approach to the Elastic Characterization.* Macromolecules, 2006. **39**(13): p. 4547-4556.

69.   Martin, G., et al., *Viscoelastic spectra of soft polymer interfaces obtained by noise analysis of AFM cantilevers.* Surface and Interface Analysis, 1999. **27**(5-6): p. 572-577.

70.   Hou, H.Y., N.K. Chang, and S.H. Chang, *Dynamic Indentation of Polymers Using the Atomic Force Microscope*, in *Nanomechanics of Materials and Structures*. 2006. p. 171-180.

71.   Nan, Y. and et al., *Frequency-dependent viscoelasticity measurement by atomic force microscopy.* Measurement Science and Technology, 2009. **20**(2): p. 025703.

72.   Mahaffy, R.E., et al., *Scanning probe-based frequency-dependent microrheology of polymer gels and biological cells.* Physical Review Letters, 2000. **85**(4): p. 880-883.

73.   Chizhik, S.A., et al., *Micromechanical properties of elastic polymeric materials as probed by scanning force microscopy.* Langmuir, 1998. **14**(10): p. 2606-2609.

74.   Wang, Y. and J.J. Santiago-Aviles, *Low-temperature electronic properties of electrospun PAN-derived carbon nanofiber.* IEEE Transactions on Nanotechnology, 2004. **3**(2): p. 221-224.

75.   Mathew, G., et al., *Preparation and characterization of properties of electrospun poly (butylene terephthalate) nanofibers filled with carbon nanotubes.* Polymer Testing, 2005. **24**(6): p. 712-717.

76.   Tomasetti, E., R. Legras, and B. Nysten, *Quantitative approach towards the measurement of polypropylene/(ethylene-propylene) copolymer blends surface elastic properties by AFM.* Nanotechnology, 1998. **9**: p. 305-315.

77.   Vandamme, M. and F.J. Ulm, *Viscoelastic solutions for conical indentation.* International Journal of Solids and Structures, 2006. **43**(10): p. 3142-3165.

78.   Chemicals, A., *LOTADER 2210-3200-3210 Safety Sheet*. 2004.

79. Pottiger, M.T. and R.L. Laurence, *The P-V-T behavior of polymeric liquids represented by the Sanchez-Lacombe equation of state* Journal of Polymer Science: Polymer Physics Edition, 1984. **22**(5): p. 903-907.

80. Sato, Y., et al., *Prediction of PVT properties of polymer melts with a new group-contribution equation of state.* Fluid Phase Equilibria, 1998. **144**(1-2): p. 427-440.

81. Pethrick, R.A., *Book review: Standard pressure-volume-temperature data for polymers. P. Zoller and D. J. Walsh. Technomic Publishing AG, Basel, 1995. pp. ix+412, price, SFr466.00. ISBN 1-56676-328-2.* Polymer International, 1997. **44**(2): p. 214.

82. Zoller, P. and D.J. Walsh, *Standard pressure - volume - temperature data for polymers*. 1995, Lancaster, Pa: technomic publ. co.

83. Ai-Bing, Y., *Johnson's SB Distribution Function as Applied in the Mathematical Representation of Particle Size Distributions. Part 2: Application of numerical results.* Particle and Particle Systems Characterization, 1994. **11**(5): p. 367-374.

84. Johnson, N.L., *Systems of Frequency Curves Generated By Methods of Translation.* Biometrika, 1949. **36**(1-2): p. 149-176.

85. Flynn, M.R., *On the Moments of the 4-Parameter Lognormal Distribution.* Communications in Statistics - Theory and Methods, 2005. **34**(4): p. 745 - 751.

86. Jian-Feng, Z., Y. Dong-Zhi, and N. Jun, *Effect of electric potential and coulombic interactions on electrospinning nanofiber distribution.* Polymer International, 2008. **57**(10): p. 1194-1197.

87. Feynman, R.P., R.B. Leighton, and M. Sands, *The Feynman Lectures on Physics*. Vol. 1. 1964, Reading.

88. Zhmayev, E., H. Zhou, and Y.L. Joo, *Modeling of non-isothermal polymer jets in melt electrospinning.* Journal of Non-Newtonian Fluid Mechanics, 2008. **153**(2-3): p. 95-108.

89. Ji-Huan He, Y.-Q.W., Jian-Yong Yub, *Allometric Scaling and Instability in Electrospinning.* Freund Publishing House Ltd, 2004. **5**(3): p. 243-252.

90.   Cheng, L. and X.G. Jian, *Synthesis of new soluble aromatic poly(amide imide)s from unsymmetrical extended diamine containing phthalazinone moiety.* Journal of Applied Polymer Science, 2004. **92**(3): p. 1516-1520.

91.   Lin, D., W. Pan, and H. Wu, *Luminescent properties of aluminum doped zinc oxide nanofibers prepared by electrospinning.* Key Engineering Materials, 2007. **336-338 III**: p. 2173-2175.

92.   D.Hoffman, J. and J. J.Weeks, J Res Natl Bur Std, 1962. **66A**: p. 13.

93.   P. P. Gan, D.R.P., *Phase behavior of blends of styrene/maleic anhydride copolymers.* Journal of Applied Polymer Science, 1994. **54**(3): p. 317-331.

VITA

PERSONAL INFORMATION
Surname, Name   :Biber, Erkan
Nationality: :Turkish (TC)
Date and Place of Birth: :April 16, 1979, İstanbul

EDUCATION

Degree	Institution	Year of Graduation
High School	Kabataş Boys High School	1997
BS	YTU, Mechanical Eng.	2001
MS	YTU, Manuf. Tech.	2004

WORK EXPERIENCE

Year	Place	Enrollment
2001-2002	Mispa Elektronik Kart. TIC	Mech. Engineer
2002-2006	YTU, Mechanical Eng. Dept.	Research Asst.
2008-2010	Çankaya U., Ind. Eng. Dept	Doc. Fell.

FOREIGN LANGUAGES

English, Spanish, German

AWARDS

Middle East Technical University, Institute of Natural Science, The best performance award, 2006

PUBLICATIONS

1. Biber E, Gündüz G, Mavis B, and Colak U, "Compatibility analysis of Nylon 6 and poly(ethylene-n-butyl acrylate-maleic anhydride) elastomer blends using isothermal crystallization kinetics" (accepted for publication in Mat. Chem. Phys. 2010)

2. Biber E, Gündüz G, Mavis B, and Colak U, "Effects of electrospinning process parameters on nanofibers obtained from Nylon 6 and poly (ethylene-n-butyl acrylate-maleic anhydride) elastomer blends using Johnson SB statistical distribution function" (accepted for publication in App. Phys. 2010)

PRESENTATIONS

1. Biber E, Gündüz G, Mavis B, and Colak U "Effect of Process Parameters on the Morphology of Electrospun Polymeric Nanofibers" The 10th Pacific Polymer Conference – PPC 10 Society of Polymer Science Kobe, Japan, 04-07 December 2007,

2. Biber E, Gündüz G, Mavis B, and Colak U "Effect of Process Parameters in Electrospiing of Polymeric Nanofibers" Nanotr III Conference Nanoteknoloji Enstitüsü Ankara, Turkey 11-14 June 2007

3. Biber E, Gündüz G, Mavis B, and Colak U "Kompozitlerin elektro eğirme (electro spinning) yontemi ile elde edilen polimerik nano elyafların polimerik kompozitlerde kullanımı ve karakterizasyonu" 1. Polimerik Kompozitler Kongre ve Sergisi Kimya Muhendisleri Odası İzmir, Turkey 17-19 November 2006

4. Biber E, Gündüz G, Mavis B, and Colak U "Kompozitlerin elektro eğirme (electro spinning) yontemi ile elde edilen polimerik nano elyafların polimerik kompozitlerde kullanımı ve karakterizasyonu" 1. Polimerik Kompozitler Kongre ve Sergisi Kimya Muhendisleri Odası İzmir, Turkey 17-19 November 2006

5. Biber E, Gündüz G, Mavis B, and Colak U "Elektro eğirme (electrospinning) yontemi ile elde edilen nano elyafların karakterizasyonları" 1. Ulusal Polimer Bilmi ve Teknolojisi Kongresi Polimer Bilmi ve Teknolojisi Derneği Ankara Turkey 21-23 June 2006